

THE IMPACT OF SEA-SPRAY DROPLETS ON THE SURFACE ENERGY
BUDGET UNDER HIGH WIND SPEEDS OVER WAVES

Final Report

N00014-95-1-0021

James B. Edson
Applied Ocean Physics and Engineering Department
Woods Hole Oceanographic Institution
Woods Hole, MA 02543

DESTINATOR STATEMENT A
Approved for public release
Distribution Unlimited

Prepared for:

Grant Monitor: Edwin P. Rood
Materials S&T Division
Office of Naval Research

19971124 022

1 November 1997

DTIC QUALITY INSPECTED 2

Table of Contents

1. Introduction	1
2. Spray droplet modeling 2. An interactive Eulerian-Lagrangian model of evaporating spray droplets.	3
3. Modeling the role of sea spray on air-sea heat and moisture exchange.	18
4. Energy flux and dissipation profiles in the marine surface layer.	20
5. Structure of the atmospheric surface layer over the ocean waves - Phase averaging via the Hilbert transform	22
6. Continuing work on the simulation of the flow of air over ocean waves.	24

1. Introduction

The research conducted under N00014-95-1-0021 investigated the influence of evaporating sea-spray under high wind conditions. These investigations were accomplished using a interactive Eulerian-Lagrangian model developed by the principle investigator. During the first year of the project, the interactive model was validated using data collected during the 1988 Couche Limite Unidimensionnelle Stationnaire (CLUSE) program. These efforts were reported in "Spray Droplet Modeling, II: An Interactive Eulerian-Lagrangian model of Evaporating Spray Droplets" by Edson et al. in the *Journal of Geophysical Research*. This work has demonstrated that the combined model accurately simulates the turbulent transport of evaporating droplets. In additions, this paper advanced the state-of-the-art in droplet research by demonstrating that the potential for substantial modification of the surface energy budget exists if the presence of waves acts to eject the droplets higher and/or disperse the droplets more efficiently.

This demonstration was taken several steps further in an abstract presented at the 12th *Symposium on Boundary Layers and Turbulence* entitled "Modeling the Role of Sea Spray on Air-Sea Heat and Moisture Exchange" by Edson and Andreas. This abstract compared the results from the interactive model with a model developed by Dr. Edgar Andreas of the U.S. Army's Cold Regions Research and Engineering Laboratory. The agreement between these models was excellent and both predicted that the contribution of the sea spray on the latent heat flux is at least 10% of the total under high wind speed conditions.

The second part of this investigation has involved modifications to the Eulerian portion of the code to include a wavy lower boundary. The validation of this model is being accomplished through comparisons with an open ocean data set collected aboard the R/P FLIP during the second part of the 1995 Marine Boundary Layers (MBL) Main Experiment. The preliminary analyses of these data have generated a great deal of interest in the modeling community, particularly because they questions a number of earlier simulations that resulted in a wave boundary layer (WBL) that extended only a few meters above the surface. Our observations indicate that the wave's influence often extended beyond the height of our upper most sensors at 18 m. A sample of these observations and the some of the analysis techniques we are developing to explain them are given sections 4 and 5.

These observations have led the PI to develop new boundary conditions and closure schemes to simulate the flow over waves as realistically as possible. These schemes are summarized in the final section, which describes the PI's work in progress. The goal of this work is to validate these schemes with the FLIP observations. The coupled model with them to examine the influence of waves on sea spray dispersion.

Spray droplet modeling

2. An interactive Eulerian-Lagrangian model of evaporating spray droplets

J. B. Edson

Woods Hole Oceanographic Institution, Woods Hole, Massachusetts

S. Anquetin

Laboratoire des Ecoulements Géophysiques et Industriels, Université Joseph Fourier, Grenoble, France

P. G. Mestayer and J. F. Sini

Laboratoire de Mécanique des Fluides, Ecole Centrale de Nantes, Nantes, France

Abstract. This paper describes an interactive Eulerian-Lagrangian model of the turbulent transport of evaporating droplets. A $k-\epsilon$ (where k is turbulent kinetic energy and ϵ is its rate of dissipation) turbulence closure model is used to accurately simulate stable, near-neutral, and unstable boundary layers within the large air-sea interaction tunnel at the Institut de Mécanique Statistique de la Turbulence (IMST), Luminy, France. These results are then used with the Lagrangian model described in part 1 [Edson and Fairall, 1994]. The coupled model is shown to give excellent agreement with droplet dispersion measurements made during the 1988 Couche Limite Unidimensionnelle Stationnaire d'Embruns (CLUSE, a French acronym that translates to one-dimensional stationary droplet boundary layer) campaign. Additionally, this paper describes how the coupled model can now be used to investigate the interaction between the evaporating droplets and the turbulent fields of temperature and humidity. The investigation shows that although the influence of the droplets is small under the conditions simulated at IMST, the potential for substantial modification of the surface energy budget exists for high-wind conditions over the ocean.

1. Introduction

This paper describes an interactive Eulerian-Lagrangian model of the turbulent transport of evaporating spray droplets. The model has been developed to address some of the limitations described by Edson and Fairall [1994] (hereinafter referred to as part 1), and to allow the use of the model in more complicated flows. The model development involved the integration of the Lagrangian model described in part 1 with an Eulerian model of turbulent flows that uses prognostic equations for the evolution of the turbulent kinetic energy k and its rate of dissipation ϵ . The integrated code has been christened Gwaihir, and we shall refer to the model as such in the following discussion.

The initial tests of the $k-\epsilon$ model are conducted through simulations of developing boundary layers using a two-dimensional version of the code. The model runs are initialized and

compared with measurements taken within the large air-water interaction simulation tunnel at the Institut de Mécanique Statistique de la Turbulence (IMST), Luminy, France, during the 1988 Couche Limite Unidimensionnelle Stationnaire d'Embruns (CLUSE, a French acronym that translates to one-dimensional stationary droplet boundary layer) campaign [Mestayer et al., 1990]. These simulations have provided a means to test the various droplet dispersion aspects of Gwaihir, as well as the performance of the Eulerian code in simulations of the marine atmospheric surface layer.

The paper describes in some detail both the physical model and the numerical procedure used in our approach. It also addresses some of the advantages of this combined (Eulerian plus Lagrangian) approach over separate approaches (Eulerian or Lagrangian) in simulations of the turbulent transport of heavy particles. It then concludes with the results from the interactive model for simulations of droplet dispersion in both a laboratory and marine atmospheric surface layer.

2. Eulerian $k-\epsilon$ Model

The Eulerian code used in this simulation is derived from a $k-\epsilon$ model developed at the Laboratoire de Mécanique des Fluids,

Ecole Centrale de Nantes, France, to simulate flows around urban structures [Lévi Alvarès *et al.*, 1990; Lévi Alvarès and Sini, 1992; Lakehal *et al.*, 1996]. In the atmospheric surface layer, expressions for the instantaneous velocity field for incompressible fluid flow can be written

$$\frac{\partial \bar{U}_j}{\partial x_j} = 0 \quad (1)$$

$$\frac{\partial U_i}{\partial t} + U_j \frac{\partial U_i}{\partial x_j} = -\frac{1}{\rho_a} \frac{\partial P}{\partial x_i} - g_i \frac{\Theta_v - \Theta_v^r}{\Theta_v^r} + v \frac{\partial^2 U_i}{\partial x_j^2} \quad (2)$$

where Einstein's summation notation is used and the Boussinesq approximation has been applied, v is the kinematic viscosity; Θ_v is the ambient virtual potential temperature; $g_i = (0, 0, -g)$ where g is the gravitational acceleration; and ρ_a and Θ_v^r and virtual potential temperature of the reference state of the fluid, respectively [Landahl and Mollo-Christensen, 1986]. In (2) the pressure field P represents the departure from the reference pressure field in hydrostatic balance. In developing equations designed to study flows where the mean departure from hydrostatic equilibrium can be nonzero (e.g., around a building), Sini [1986] and Sini and Dekeyser [1987] decomposed this departure from hydrostatic equilibrium into mean and fluctuating parts. The Reynolds averaged equations for the mean variables are then given by

$$\frac{\partial \bar{U}_j}{\partial x_j} = 0 \quad (3)$$

$$\frac{\partial \bar{U}_i}{\partial t} + \bar{U}_j \frac{\partial \bar{U}_i}{\partial x_j} = -\frac{1}{\rho_a} \frac{\partial \bar{P}}{\partial x_i} - g_i \frac{\bar{\Theta}_v - \bar{\Theta}_v^r}{\bar{\Theta}_v^r} - \frac{\partial \bar{u}_i \bar{u}_j}{\partial x_j} + v \frac{\partial^2 \bar{U}_i}{\partial x_j^2} \quad (4)$$

$$\frac{\partial \bar{\Theta}}{\partial t} + \bar{U}_j \frac{\partial \bar{\Theta}}{\partial x_j} = \frac{\partial \bar{u}_j \bar{\Theta}}{\partial x_j} + \frac{S_H}{\rho_a c_p} \quad (5)$$

$$\frac{\partial \bar{Q}}{\partial t} + \bar{U}_j \frac{\partial \bar{Q}}{\partial x_j} = \frac{\partial \bar{u}_j \bar{q}}{\partial x_j} + S_q \quad (6)$$

where the overbar represents an ensemble average; lower case letters denote the turbulent fluctuations; the total specific humidity Q has since been added to allow for the inclusion of moisture in the model equations; c_p is the specific heat at constant pressure; and S_H and S_q represent source terms for sensible heat and moisture, respectively. The source/sink terms are discussed in detail below.

2.1. Closure

The Reynolds-stress tensor is modeled using the Boussinesq eddy diffusivity concept

$$-\bar{u}_i \bar{u}_j = v_T \left[\frac{\partial \bar{U}_i}{\partial x_j} + \frac{\partial \bar{U}_j}{\partial x_i} \right] - \frac{2}{3} \delta_{ij} k \quad (7)$$

where δ_{ij} is the Krönecker delta tensor, v_T is the eddy diffusivity, and k is the turbulent kinetic energy (TKE) defined as

$$k = \frac{1}{2} \bar{u}_j \bar{u}_j \quad (8)$$

Similarly, the scalar fluxes are modeled using

$$-\bar{u}_j \bar{\Theta} = K_\Theta \frac{\partial \bar{\Theta}}{\partial x_j} \quad (9)$$

$$-\bar{u}_j \bar{q} = K_q \frac{\partial \bar{Q}}{\partial x_j} \quad (10)$$

where K_Θ and K_q are the exchange coefficients for potential temperature and specific humidity, respectively. The exchange coefficients are parameterized as

$$v_T = C_\mu \frac{k^2}{\epsilon} \quad (11)$$

$$K_\Theta = Pr_T v_T \quad (12)$$

$$K_q = Sc_T v_T \quad (13)$$

where C_μ is a model coefficient and the Prandtl and Schmidt numbers for turbulent diffusion are assigned the same value, $Pr_T = Sc_T = 0.95$ [Högström, 1988].

Closure is then accomplished through prognostic equations for both the turbulent kinetic energy and its rate of dissipation

$$\begin{aligned} \frac{\partial k}{\partial t} + \bar{U}_j \frac{\partial k}{\partial x_j} = & \frac{\partial k}{\partial t} + \bar{U}_j \frac{\partial k}{\partial x_j} = \\ -\bar{u}_i \bar{u}_j \frac{\partial \bar{U}_i}{\partial x_j} - \frac{g_j}{\Theta_v} \bar{u}_j \bar{\Theta}_v + \frac{\partial}{\partial x_j} \left[\frac{v_T \partial k}{\sigma_k \partial x_j} \right] - \epsilon & (14) \end{aligned}$$

$$\begin{aligned} \frac{\partial \epsilon}{\partial t} + \bar{U}_j \frac{\partial \epsilon}{\partial x_j} = & -C_{\epsilon 1} \frac{\epsilon}{k} \left[\bar{u}_i \bar{u}_j \frac{\partial \bar{U}_i}{\partial x_j} + \frac{g_j}{\Theta_v} \bar{u}_j \bar{\Theta}_v \right] \\ + \frac{\partial}{\partial x_j} \left[\frac{v_T \partial \epsilon}{\sigma_\epsilon \partial x_j} \right] - C_{\epsilon 2} \frac{\epsilon^2}{k} & (15) \end{aligned}$$

where ϵ is the rate of irreversible dissipation of kinetic energy into thermal energy and σ_k , $C_{\epsilon 1}$, σ_ϵ , and $C_{\epsilon 2}$ are model coefficients. By parameterizing the transfer coefficients in this fashion, we believe that the diffusive properties of the flow are more representative of the intensity k and persistence k/ϵ of the turbulence than could be obtained through the normal application of first-order closure (i.e., K -theory). The two-equation approach is also less complicated and less expensive to run than higher-order models, while still maintaining many of their advantages over those of first order or those that assume a balance between production and dissipation of TKE.

2.2. Model Coefficients

The numerical coefficients are chosen such that they are representative of the laboratory boundary layer (LBL) at IMST. The values of the coefficients σ_ϵ , $C_{\epsilon 1}$, and $C_{\epsilon 2}$ are based on semiempirical relationships [e.g., Avva *et al.*, 1988; Duynkerke, 1988]. These relationships have been shown to be in good agreement with observation made within the air-sea interaction tunnel at IMST [Mestayer, 1980]. In particular, the near-surface dissipation rate is well defined in neutral conditions by

$$\epsilon = \frac{u_*^3}{\kappa z} \quad (16)$$

where u_* is the velocity scaling parameter (or more commonly the friction velocity) and the von Karman's constant, κ , is assigned a value of 0.4 [Högström, 1988].

We use the measurements of Mestayer [1980] to relate the friction velocity to vertical velocity variance as $\sigma_w^2 = 1.69 u_*^2$. The constant of proportionality C_μ used in (11) to define the eddy diffusivity, is assigned the value 0.09. This value has been successfully used to simulate a number of laboratory flows [e.g., Launder and Spalding, 1974]. The value of $C_{\epsilon 2}$ is found from measurements taken in homogeneous grid turbulence where the diffusion and production of TKE are negligible. This leads to a situation where there exists a balance between the advection and dissipation of TKE such that $C_{\epsilon 2}$ becomes the only constant of significance in (14) and (15). Values of $C_{\epsilon 2}$ determined from these measurements are found to lie within the range of 1.8 to 2.0 [Avva *et al.*, 1988]; we have chosen the commonly used value of 1.92 for the present model. In highly stratified flows, where the Richardson number has reached its critical value Ri_c , the transport processes again become negligible and (14) and (15) can be combined to give [Duynkerke, 1988]

$$C_{\epsilon 1} = C_{\epsilon 2}(1 - Ri_c) \quad (17)$$

Additionally, near the surface, where we expect a balance between mechanical production and dissipation of TKE, a logarithmic velocity profile, and negligible transport, (15) reduces to

$$C_{\epsilon 1} = C_{\epsilon 2} - \frac{\kappa^2}{\sigma_\epsilon C_\mu^{1/2}} \quad (18)$$

Table 1. Numerical Constants Used in the Model Simulations

Constant	Value
C_μ	0.09
$C_{\epsilon 1}$	1.44
$C_{\epsilon 2}$	1.92
σ_k	1.00
σ_ϵ	1.11
κ	0.40
Pr_T	0.95
Sc_T	0.95

See section 2.1 for variable definitions.

Equations (17) and (18) can then be combined to obtain

$$\sigma_\epsilon = \frac{\kappa^2}{C_\mu^{1/2} C_{\epsilon 2} Ri_c} \quad (19)$$

In the present model we have assigned the values 1.0 and 0.25 to σ_k and Ri_c , respectively. Using these values and the above expressions we obtain the values of the coefficients listed in Table 1.

2.3. Numerical Formulation

The numerical formulation is an adaptation of the code Chensi developed by Lévi Alvarès [1992] and Lévi Alvarès and Sini [1992] for an inhomogeneous, three-dimensional (3-D) grid. The solution of the system of equations is found using the Marker-and-Cell computing method as presented by Hirt and Harlow [1967]. The numerical model utilizes a staggered grid configuration that defines the velocity components at the cell faces and the scalar variables at the cell centers as shown in Figure 1. Variable grid spacing is used to allow for smaller grid increments in regions where strong gradients are expected, in an effort to reduce the numerical noise in the algorithm. The derivatives are determined with a second-order, finite volume scheme that takes into account the variable grid spacing as described by Lévi Alvarès [1992].

The numerical method is explicit in time and uses an upwind weighted difference scheme for the advection terms and a centered difference scheme for the diffusion terms. The continuity equation is satisfied for the mean velocities at each time step through use of the artificial compressibility method described by Chorin [1967]. The system of equations is then marched forward in time until the desired level of convergence is reached such that the Eulerian variables represent the steady state solution. In the current model we assume that a steady state has been reached when changes in model parameters between successive time steps approach the computer's

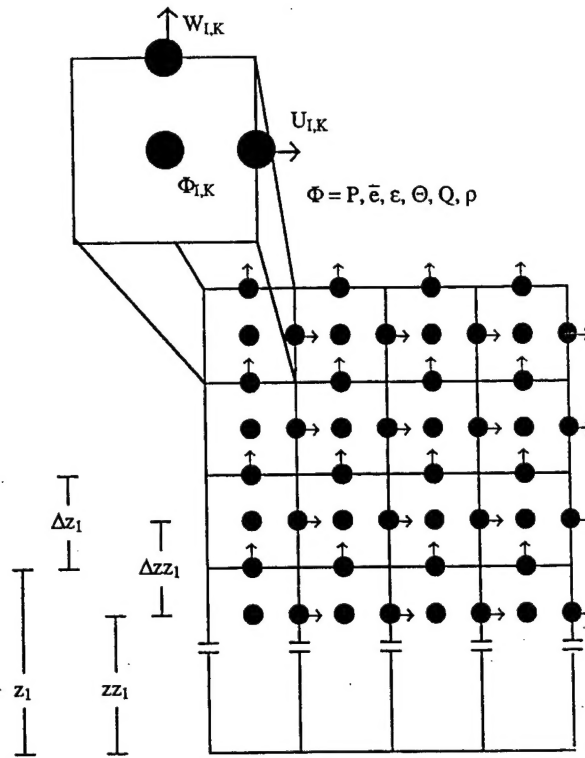


Figure 1. The staggered grid configuration used in the Eulerian model.

numerical precision (currently, a Sun Sparcstation 2 using double precision).

In the simulations that follow the height of the lowest grid point is set to 1 cm. Therefore it is safe to assume that molecular effects can be neglected since this height is at least an order of magnitude larger than the roughness length z_o . The 2-D domain of the model simulations measures 50 m by 0.85 m, which is roughly the length and height, respectively, of the turbulent boundary layer at IMST. The determination of the boundary conditions using the configuration shown in Figure 1 is discussed in some detail below.

2.4. The Boundary Conditions

In the $k-\varepsilon$ code we define the grid as shown in Figure 1, where the parameters in the first grid are not defined at its center. This approach saves computer time and improves the determination of the derivatives at the lowest grid points. It also allows us to move the height of the first grid point to a region well above the viscous sublayer such that we can safely ignore molecular effects. However, these noncentered grid points found in the first cells require special consideration. The velocity component parallel to the surface (in these simulations the horizontal velocity) is found using the wall law given by *Launder and Spalding* [1974] to estimate the surface stress

$$u_*^2 = \frac{\tau_o}{\rho_a} = \frac{\kappa(\bar{U}_2 - \bar{U}_o)C_p^{1/4}k^{1/2}}{\ln\left(\frac{zz_2}{z_o}\right)} \quad (20)$$

where the subscripts o and 2 represent the values at z_o and at the second grid point, respectively. Equation (20) reduces to the classic logarithmic profile when a constant stress layer prevails near the surface; that is, we assume that

$$u_* = C_p^{1/4}k^{1/2} \quad (21)$$

The roughness length at the end of the tunnel is estimated from

$$z_o|_{I_{\max}} = \frac{v}{C_z C_p^{1/4} k_{I_{\max},2}^{1/2}} + \frac{C_g C_p^{1/2} k_{I_{\max}}}{g} \quad (22)$$

where the I_{\max} denotes the value at the outflow section of the model domain. The first term on the right-hand side of (22) gives the roughness length for a smooth surface with $C_z = 9$, while the second term is based on Charnock's formula [Charnock, 1955] using $C_g = 0.017$ [Garratt, 1977]. The value of z_o at the lowest grid point in the inflow section is assumed to equal that for a smooth surface. Using these two values, we then assume that the surface roughness increases in a linear fashion with fetch. This assumption is consistent with actual measurements made within the tunnel.

The vertical velocity at the lowest grid points is then determined by requiring that the continuity equation is satisfied in the lowest cells. First, the average horizontal velocity through each grid face U_I is found by integrating the log profile from z_o to z_1 . The vertical velocity is then found using (3), with $W_o = 0$, such that

$$W_1 = -\frac{U_I - U_{I-1}}{\Delta x} (z_1 - z_o) \quad (23)$$

where Δx is the width of each cell.

A condition of zero diffusive flux of TKE is used between the first two grid points

$$\left(\frac{\partial k}{\partial z} \right)_{1,2} = 0 \quad (24)$$

The dissipation rate of TKE is found by assuming that the mechanical production of TKE is equal to dissipation in the near-wall region. This leads to a relationship between the TKE and its dissipation rate at the lowest grid point given by

$$\epsilon_1 = \frac{(C_p^{1/4}k^{1/2})^3}{\kappa z z_1} \quad (25)$$

The horizontal velocity profile at the upstream boundary (hereafter referred to as the entrance) is fixed using a profile based on the measurements made by *Selva* [1979] in the IMST tunnel using a Pitot tube and highly accurate manometer. Neumann conditions (i.e., zero gradient) are used for all variables at the upper and downstream boundaries, except for the vertical velocity at the upper boundary, which is set equal to zero.

The initial values of k are found by inversion of (21), while initial values of ϵ are assigned using (16). The value of u_* used in both relationships is assigned an initial value equal to two fifths the value of u_* measured at a distance (fetch) of 30 m from the tunnel entrance. The inflow values of k and ϵ are then allowed to adjust through the use of Neumann conditions. The temperature and specific humidity profiles at the tunnel entrance are fixed using the value measured at 0.75 m, except for at the lowest grid point that is given the surface value. This is consistent with both measurements and the action of the heat exchangers in the tunnel, which act to hold the air temperature and dew point constant, mix the air thoroughly, and break down any undesirable eddies. At the lower boundary the temperature is given the value of the water surface temperature T_w , while the specific humidity is assigned its saturation value at T_w .

2.5. Eulerian Model Results

The Eulerian model's velocity results are in good agreement with the measurements made using a Pitot tube during the CLUSE campaign as shown in Figure 2. The various curves in Figure 2 depict the evolution of the wind profile at various fetches. The velocity profile measured at 30 m gives excellent agreement with the model profile at a fetch of 29 m. This result indicates that the velocity evolution is accurately modeled, especially since there is some uncertainty as to where we define the fetch to be equal to 0. The small discrepancy between the model and measurements at the top of the boundary layer is the result of the confluence of the tunnel's two boundary layers.

In general, the vertical structure of temperature and humidity along the length of the tunnel cannot be adequately described

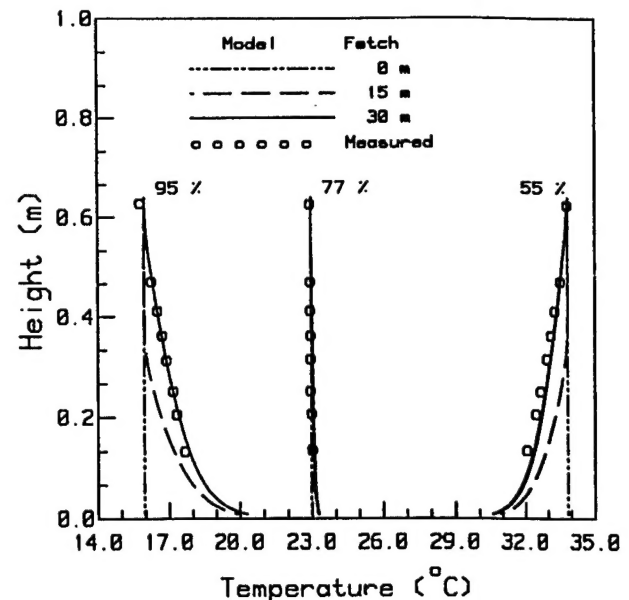


Figure 3. A comparison of the temperature measurements made at a fetch of 30 m in the IMST tunnel with the Eulerian model results. The three sets of data are representative of the high-, medium-, and low- humidity (95%, 77%, and 55%, respectively) runs made during CLUSE. The nominal wind speed in all three cases is approximately 7.5 m s^{-1} . The group of curves depicts the model-derived temperature profiles at the fetches indicated. The standard deviation of the measured temperature variance is given at each level for the medium humidity run.

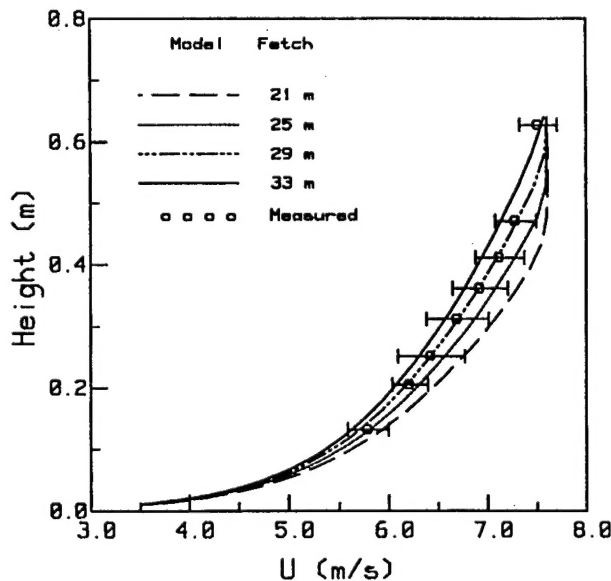


Figure 2. A comparison of the velocity measurements made at a fetch of 30 m in the Institut de Mécanique Statistique de la Turbulence (IMST) tunnel with the Eulerian model results. The group of curves depicts the model-derived wind profiles at the fetches indicated. The error bars denote the standard deviation of the measured velocity variance.

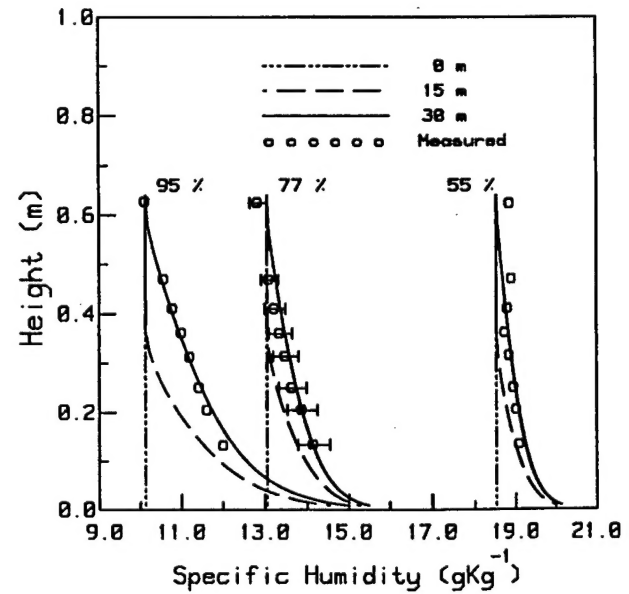


Figure 4. A comparison of the specific humidity measurements made at a fetch of 30 m in the IMST tunnel with the Eulerian model results. The conditions are the same as in Figure 3. The standard deviation of the measured specific humidity variance is given at each level for the medium humidity run.

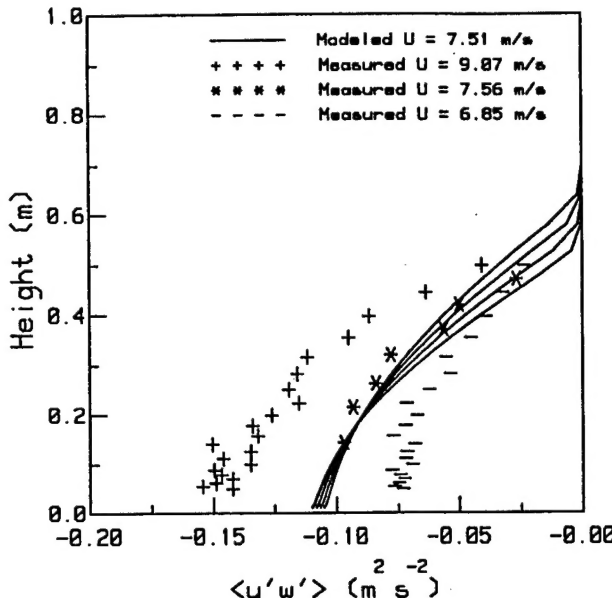


Figure 5. A comparison of the momentum flux measured at the indicated wind speeds at a fetch of 30 m in the IMST tunnel with the Eulerian model results. The group of curves depicts the growth of the simulated boundary layer through flux profiles determined at 27, 29, 31, and 33 m (from right to left, looking at the top of the curves) for a wind speed of 7.5 m s^{-1} .

by single profiles as used in part 1 (even without the droplets). Owing to the mixing of the air by the turboprop and heat exchangers, the air enters the test section with approximately constant values of specific humidity and temperature. As the air moves along the length of the tunnel, it interacts with the water surface through molecular and eddy exchange. This interaction is shown in Figures 3 and 4, which indicate good agreement between measured and modeled results at a fetch of 30 m. These measurements were made using a thermocouple psychrometer system provided by the University of Washington using chromel constantan thermocouples. These devices are believed to be accurate to $\pm 0.2^\circ\text{C}$; however, cold spikes caused by droplets impacting the sensors are expected to increase the uncertainty in these measurements [Katsaros *et al.*, 1994].

The result of primary interest for droplet dispersion is shown in Figure 5, which displays the $-uw$ component of the Reynolds-stress tensor computed from

$$-\overline{uw} = v_T \frac{\partial \bar{U}}{\partial z} \quad (26)$$

with carefully conducted measurements made at a fetch of 30 m over a range of wind speeds by *Giovanangeli and LeCalve* [1990] at IMST. The group of curves representing the model results at several fetches shows that the model gives good agreement with the measurements made at the same wind speed at a fetch of 30 m. These curves are representative of a developing LBL and indicate that the growing surface layer reaches a height of approximately 0.2 m at 30 m. The implications of this developing surface layer on droplet dispersion is addressed in section 3.

3. Droplet Dispersion Modeling

Several Eulerian approaches have been successfully applied to the study of turbulent diffusion of discrete particles in boundary layer flows. These include the studies of *Ling and Kao* [1976], *Ling et al.* [1978, 1980], *Burk* [1984], *Mostafa and Mongia* [1987], *Stramska* [1987], and *Rouault et al.* [1991], among others. However, the restraints placed on these models often restrict their application to either very small, highly concentrated particles or simple flow geometries with a homogeneous source of particles that can then be studied using budget equations.

Note that these constraints are not always a drawback. For example, in highly concentrated flows, where the particle-particle interactions are not negligible, it is generally much easier to include these effects in a Eulerian scheme than a Lagrangian one. Additionally, the use of budget equations can provide a means of studying the effects of particle interaction with the scalar fields through the use of source/sink relationships, which are difficult to include in a purely Lagrangian scheme. This approach has been successfully employed by *Rouault et al.* [1991], who studied the effect of droplet evaporation on the scalar fields of temperature and humidity.

The simulation of the movement of heavy particles involves parameterizations to account for the effects of gravity and inertia. These parameterizations generally require the tuning of adjustable constants through comparison with experimental data [e.g., *Rouault et al.*, 1991]. Unfortunately, these calibration measurements are difficult to come by, several notable exceptions being the studies of *Snyder and Lumley* [1971] and the Humidity Exchange Over the Sea (HEXOS) in a Simulation Tunnel (HEXIST) experiments [e.g., *Andreas et al.*, 1995]. There is also a question as to the universality of these constants when they are applied to more complicated flows. Finally, as in any Eulerian model, discrete sources of particles are difficult to include in the calculation domain and generally require subgrid-scale parameterizations that are often difficult to quantify.

Therefore we feel that the Lagrangian approach is the best alternative if one is concerned with the dispersion of low-concentration, heavy particles from discrete or nonuniform sources (e.g., from spume droplets produced at the wave crests) and in fluid flows with complicated geometries (e.g., over waves or within a surf zone). The approach also allows for much more flexibility in specifying boundary conditions. For example, a Lagrangian scheme can easily include boundary conditions where the particles either rebound or stick, depending on the type of surface one is trying to simulate. It is also especially advantageous in situations where the physicochemical characteristics of the particles change rapidly when they experience a highly inhomogeneous environment. In this instance, time rate of change equations, which may depend upon the local conditions, as well as on the particle's history, are easily included in the model as long as these equations are known.

The Lagrangian model is described in detail in part 1. Briefly, the model relies on a finite difference form of the Langevin equation for the fluctuating components of the droplet's velocity due to turbulence. When the mean droplet

fall velocity \bar{W}^P is added to this fluctuating component $w^P(t)$, the instantaneous vertical velocity is given by

$$W^P(t+\Delta t) = \left(1 - \frac{\Delta t}{\tau_w^P}\right) W^P(t) + \sigma_w^P \left(\frac{2}{\tau_w^P}\right)^{1/2} \zeta(t) + \frac{\Delta t}{\tau_w^P} \bar{W}^P \quad (27)$$

where τ_w^P is the droplet integral timescale, Δt is the time step, σ_w^P is the square root of the droplet vertical velocity variance, and $\zeta(t)$ is a random number drawn from a Gaussian distribution with zero mean and variance Δt . The expressions for τ_w^P and σ_w^P are then derived from the equation of motion for small, heavy droplets given by

$$\frac{Dw^P}{Dt} = -\frac{K}{\alpha} w^R = \frac{K}{\alpha} (w^f - w^P) \quad (28)$$

where the superscripts f and R denote the fluid and relative velocities, respectively, and the total derivative denotes motion following the droplet. The parameter K represents the ratio of the Stokes velocity to the mean relative fall velocity, and α is the response time for droplets that ideally obey Stokes law.

The approach given in part 1 yields the following expression for the vertical velocity variance:

$$\sigma_w^P = \frac{\sigma_w^2}{(1 + \chi)} \quad (29)$$

where

$$\chi = \frac{\alpha}{K\tau_L} \quad (30)$$

The parameter χ is the ratio of the droplet response time to the Lagrangian integral time scale τ_L . This parameter thereby determines how the droplet reacts to the turbulent motion of the surrounding fluid, e.g., as the droplet encounters smaller eddies as it nears the surface (smaller τ_L), the influence of the turbulence on the droplet motion diminishes because the droplet can no longer react to these smaller eddies due to its inertia. The height at which this begins to occur is determined by the droplet's size as reflected by its response time α/K . The equivalent situation occurs as the turbulence intensity increases (again, smaller τ_L) such that its response time becomes too large to permit the droplet to react fast enough to all scales of the turbulence.

The integral timescale is a measure of the persistence of the droplet's velocity as it moves through the fluid. This coefficient is derived by determining the droplet autocorrelation coefficient in an approach similar to that used by *Meek and Jones* [1973]. The droplet integral timescale is then determined by integrating the autocorrelation function over time, which yields

$$\tau_w^P = \frac{\tau_L}{\Lambda} (1 + \chi) \quad (31)$$

where

$$\Lambda = \left[1 + (\bar{W}^P/\sigma_w^P)^2\right]^{1/2} \quad (32)$$

The parameter $1/\Lambda$ accounts for the decorrelating effect of the droplet falling out of a fluid parcel where the fluctuating fluid velocities are highly correlated over small time steps. In past studies this parameter has been tuned to fit experimental data by multiplying $(\bar{W}^P/\sigma_w^P)^2$ in (32) by a constant ranging between 0.3 and 1 [e.g., *Mostafa and Mongia*, 1987; *Wells and Stock*, 1983]. In this study we continue to use the formulation given in part 1; that is, the constant is left equal to 1. We address the implication of this choice in the discussion given below.

The Lagrangian integral timescale is commonly defined in engineering literature [e.g., *Mostafa and Mongia*, 1987] using the output of the $k-\epsilon$ model as $\tau_L = \beta k/\epsilon$, where β ranges between 0.15 and 0.6. If we equate this expression with the expression used in part 1, we obtain

$$\tau_L = \frac{v_T}{\sigma_w^2} = 0.18 \frac{k}{\epsilon} \quad (33)$$

The vertical velocity variance is parameterized in terms of the kinetic energy by combining (21) with the results from *Mestayer* [1980] to obtain

$$\sigma_w^2 = 1.69 C_\mu^{1/2} k \quad (34)$$

4. Gwaihir

With these parameters we have all the necessary expressions to simulate the turbulent dispersion of heavy particles once the Eulerian fields are available from the $k-\epsilon$ code. Therefore, after a steady state solution of a particular flow configuration is found, the velocity and scalar values are passed to the Lagrangian section of the code in order to determine the parameters in the above expressions. These parameterizations are then used with (27) to compute the trajectories of evaporating droplets. The amount of trajectories begun over a specified time T is determined by a user-defined source function. As these trajectories are computed, the Lagrangian code keeps track of the droplet concentration q_D , sensible heating rate S_H , and water vapor production S_q in each cell. Once the Lagrangian portion of the code has ejected all of the droplets determined by the source function over the time T , the Eulerian portion of the code is then rerun with the new nonzero values of q_D , S_q , and S_H . This process is repeated until the $k-\epsilon$ code, upon completion of the last Lagrangian run, reaches a steady state over an interval less than T .

The source of droplets is determined from the surface source function, which gives the number of droplets per unit time, per unit area produced at the surface. Since the droplet measuring devices were situated slightly downwind of the 30-m-long bubbler array used during the CLUSE campaign [*Mestayer et al.*, 1990], the Gwaihir source function was determined by matching the model output with droplet measurements made at a height of 0.2 m, 0.5 m downwind of the simulated source.

The total number of droplets over a radius interval between $r - \Delta r/2$ and $r + \Delta r/2$ ejected from a prescribed area (where Δr is the radius increment) is given by

$$N(r) = N_T(r)T\Delta r\Delta x\Delta y \quad (35)$$

where $N_T(r)$ is the surface source function, T is the total time that the source is on, Δx is the length of the area, and Δy is its width (set equal to unity in this 2-D simulation). Since Gwaihir uses a horizontal grid spacing of $\Delta x = 0.5$ m, the source is divided up into 60 sections.

The droplets produced in each section are then released at their ejection height. This height corresponds to the height to which a jet droplet is ejected by a bubble bursting. The height and number of droplets ejected are a function of bubble size, and we have used the data given by *Blanchard and Woodcock* [1957] to determine these parameters as described in part 1.

As the released droplet moves through the model domain, the values needed in the Lagrangian model parameterizations are determined from a linear average of the four nearest Eulerian grid points in order to find $U(X, Z)$, $W(X, Z)$, and $\Phi(X, Z)$ at X, Z . Owing to the staggered grid, this involves keeping track of four different indices corresponding to x, xx, z , and zz . If the droplet falls below zz_1 , the values of the variables are found using the same wall functions employed in the Eulerian model. If the droplet falls below z_o , it is assumed to stick to the surface, in which case another trajectory is begun. A new droplet trajectory is also begun if a droplet is carried out of the calculation domain.

The concentration of droplets over a specified size range is calculated by accumulating the time these droplets spend in each cell. The accumulated time, divided by the total time that the source is on, divided by the volume of the cell is a measure of the droplet concentration. The droplet volume concentration (droplet volume, per unit volume, per radius increment) in each cell is then computed from

$$\frac{dV(r)}{dr} = \frac{4}{3} \frac{\pi r^3}{VT\Delta r} \sum \Delta t \quad (36)$$

where the summation is for each cell over the advection time T , and $V = \Delta x\Delta y\Delta z$ is the volume of each cell.

The source functions of $\rho_a c_p \Theta$ and Q are the means by which the evaporating droplets interact with the fields of sensible heat and moisture. These functions can act as either a source or sink of sensible heat and moisture depending on the ambient conditions. Therefore Q in (6) is actually the total specific humidity

$$Q(x, z) = q_v(x, z) + q_L(x, z) \quad (37)$$

where q_v is the specific humidity due to water vapor and q_L is the contribution due to liquid water other than the spray droplets (e.g., fog). Here we are assuming that the fog droplets are small enough that they can be properly modeled by (6); that is, the fog droplets are small enough to be treated as passive scalars. On the other hand, the spray droplets are too large for such treatment and are instead modeled separately by the Lagrangian code.

In breaking down the specific humidity in this fashion the source/sink functions become solely a function of droplet evaporation/condensation. The interaction between the evaporating droplets and the scalar fields is then simulated by releasing all the droplets produced during a given period of time and accumulating the sensible heat and moisture they consume or release in each cell. The functions used in this model are given as

$$S_H = -\frac{4\pi}{VT} \sum r k_a f_H(T_a - T_s) \Delta t \quad (38)$$

$$S_q = -\frac{4\pi \rho_p}{VT \rho_a} \sum r^2 \frac{dr}{dt} \Delta t \quad (39)$$

where the summation is over all droplets in each cell, ρ_p is the density of the droplet, f_H is the ventilation coefficient for heat diffusion [Beard and Pruppacher, 1971], k_a is the thermal conductivity of air, and T_a and T_s are the air and droplet surface temperatures, respectively.

The evaporation rate, dr/dt , is determined using the function given by Beard and Pruppacher [1971] using modification proposed by Andreas [1989] for curvature effects, while the droplet surface temperature is governed by the functions described in part 1. The droplet surface temperature is assigned the value of the water surface at the time of its release. Initialized in this way, Gwaihir explicitly models the initial transfer of sensible heat from droplet to air when the sea surface temperature exceeds the air temperature (unstable conditions) as described by Andreas *et al.* [1995], as well as the eventual cooling (heating) of the atmosphere due to evaporation (condensation).

The virtual temperature required in (4), (14), and (15) is then determined by considering all three sources of moisture [Stull, 1988]

$$\Theta_v(x, z) = \Theta(x, z) [1 + 0.61 q_v(x, z) - q_L(x, z) - q_D(x, z)] \quad (40)$$

where q_D is the contribution to the total specific humidity from the droplets; that is, it is found by integrating the droplet volume concentration in each cell. In practice, q_L is equal to zero unless Q is greater than its saturation value. If supersaturation occurs, then $q_L(x, z)$ is equal to $q_{sat}(x, z)$ and $q_L(x, z)$ is equal to $Q(x, z) - q_{sat}(x, z)$.

These additional sources of moisture are included in the buoyancy flux using the approach given by Stull [1988]

$$\begin{aligned} \overline{w\Theta_v} &= \overline{w\Theta} [1 + 0.61 \overline{q_v} - \overline{q_L} - \overline{q_D}] \\ &+ \Theta [0.61 \overline{wq_v} - \overline{wq_L} - \overline{wq_D}] \end{aligned} \quad (41)$$

where we are ignoring the triple products found in its full derivation. The fluxes are defined by breaking down the moisture terms as described above and using

$$-\overline{wC'} = Pr_T v_T \frac{\partial C}{\partial z} \quad (42)$$

where $C = q_v, q_L, q_D$ and we assume, following *Rouault et al.* [1991], that the turbulent Prandtl and droplet Schmidt numbers are equal.

5. Gwaihir Results

In this section we concentrate on how we have addressed some of the earlier model's deficiencies by combining it with the Eulerian code. Specifically, we examine the improvement between the model and measurement comparisons due to a more realistic simulation of the turbulent field through which the droplets are dispersing. Second, we demonstrate the improvements in our simulations due to the ability of Gwaihir to permit interaction between the droplets and the scalar fields. Finally, we examine the extent to which the droplets modify the scalar fields and examine how this effect modifies the fluxes of sensible and latent heat.

5.1. Influence of the Turbulent Flow Field on Droplet Dispersion

In section 2.5 we demonstrated that the $k-\epsilon$ model is capable of accurately simulating a 2-D developing surface layer. We now examine how the improved simulation of the turbulent flow field affects the output of the Lagrangian component. In Figure 6, we begin our comparison between Gwaihir and the droplet measurements taken during the CLUSE campaign. It shows excellent agreement between Gwaihir (at a fetch corresponding to 30.5 m) and measurements for all sizes and

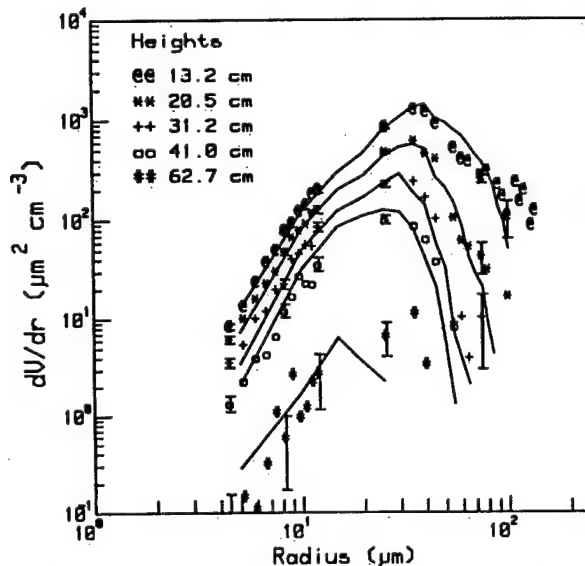


Figure 6. Droplet volume spectra as a function of droplet radius. The solid lines represent the model results, while the symbols represent data measured at the indicated heights. The error bars are computed at every fifth data point from $dV/dr \times (1 \pm 1/N)$, where N is the number of droplets counted over the size interval. The conditions during the run were a relative humidity of 95% and a nominal wind speed of 7.5 m s^{-1} .

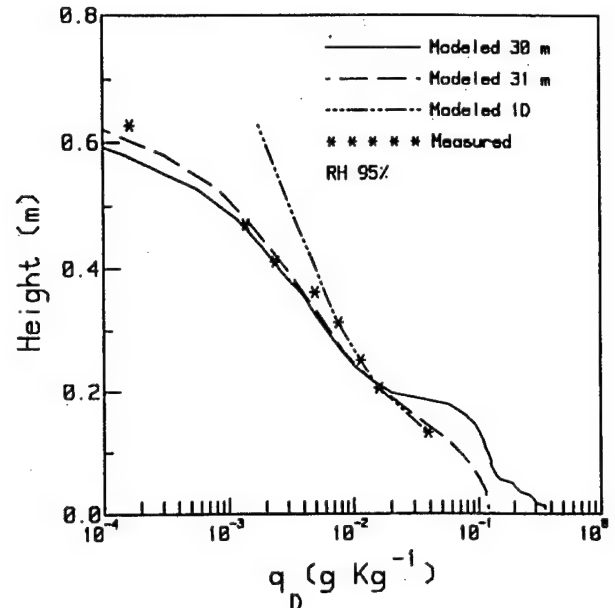


Figure 7. Profiles of total liquid water content q_D , calculated by integrating over the measured and modeled droplet spectra at each height. The symbols represent data measured at the indicated heights. The solid line represents Gwaihir results taken directly over the simulated source of droplets, while the dashed line shows the profile 1 m beyond the end of this source. The dash-dotted line reproduces the one-dimensional model results given by *Edson and Fairall* [1994]. The conditions during the run were a relative humidity of 95% and a nominal wind speed of 7.5 m s^{-1} .

heights, except for the largest droplets at 63 cm. This is perhaps a result of the merging of two boundary layers in the actual tunnel, which we have not tried to model in this simulation.

Upon close inspection of Figure 6 we see that Gwaihir is slightly underestimating the vertical dispersion of the larger droplets. The agreement between the model and measurements at the largest sizes could be improved by including a fractional constant in (32) as described above. However, its inclusion would worsen the agreement at smaller sizes. A more likely explanation for the disagreement is that we are simply pushing Gwaihir too far; that is, we are using a 1-D Lagrangian model in a 2-D flow. A better alternative is to make the Lagrangian portion of the code 2-D by including a correlated horizontal component of the droplet velocity as did *Ley and Thomson* [1983]. Additionally, the assumptions that lead to its development suggests that it works best in homogeneous turbulence, which is clearly not the case in the LBL. In fact, we expect Gwaihir to work better in simulations of a marine surface layer, where these conditions are better realized.

Even with these minor shortcomings, Figures 7 and 8 indicate that we have improved the model simulations (compared with the results given in part 1) by simply improving the simulation of the turbulent flow field, rather than trying to tune the Lagrangian model parameters. This is evident in the profiles of q_D given in Figure 7, which is computed by approximating

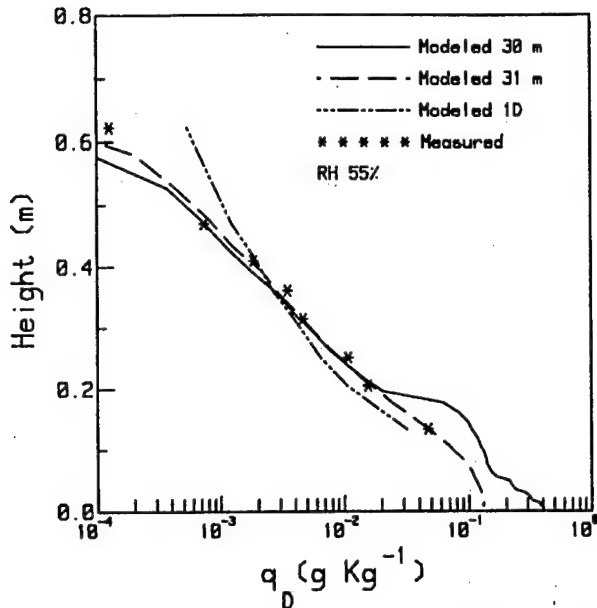


Figure 8. Profiles of total liquid water content q_D , for a relative humidity of 55% and a nominal wind speed of 7.5 m s^{-1} . The lines are as denoted in Figure 7.

the area under the curves shown in Figures 6 and 9 in part 1 using

$$q_D = \frac{\rho_p}{\rho_a} \sum_{i=1}^N \left(\frac{dV}{dr} \right)_i \Delta r_i \quad (43)$$

where N is the total number of radius increment bins and the density units are chosen to give grams per kilogram. Figure 7 shows that either version of the model gives excellent agreement with the measurements within the constant flux layer. Recall that the constant flux is assumed to exist throughout the 1-D boundary layer simulated in part 1. This is the reason why Gwaihir gives much better agreement as we near the top of the boundary layer, where the momentum flux tends toward zero, which causes a drastic reduction in the vertical dispersion of the droplets.

Figure 8 shows that Gwaihir does a better job of handling droplet evaporation than the 1-D model, which tended to overevaporate the droplets. This is due to the inclusion of droplet feedback mechanisms (i.e., the moistening of the near surface which lessens the amount of evaporation), as well as the general improvement of the mean profile simulations of temperature and moisture. In fact, this latter effect is most likely the cause for the improvement, for reasons given in section 5.2.

5.2. Influence of Droplets on the Scalar Fields

The first step in the simulation is to compute the turbulent fields of velocity, temperature, and humidity in the absence of droplets. Therefore the $k-\epsilon$ model gives us an easy way to determine the effect of droplet evaporation on the scalar fields by examining the difference in the temperature and humidity profiles modeled with and without droplets. In Figure 9 we

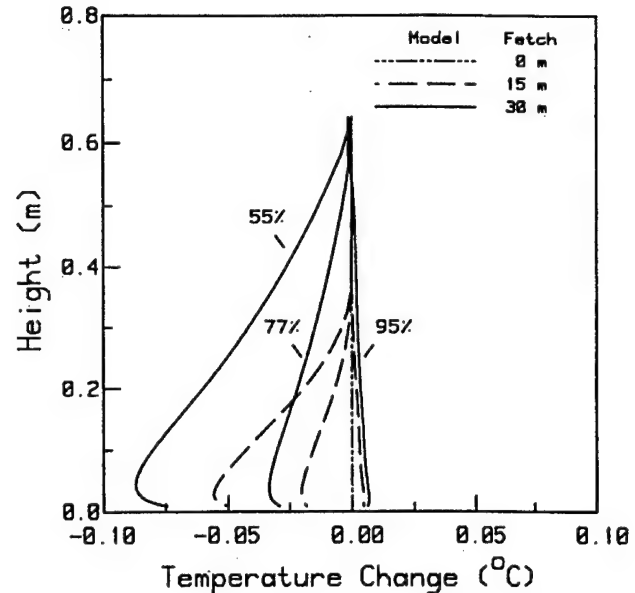


Figure 9. Profiles of the change in the model-derived temperature profiles due to the presence of droplets. The nominal wind speed was 7.5 m s^{-1} for all runs, while the relative humidity is as indicated on the profiles measured at 30 m (55%, 77%, and 95%).

depict the difference in temperature profiles due to the presence of droplets. The high humidity run in Figure 9 illustrates a case where the release of sensible heat from the droplets causes the near-surface air temperature to actually increase. This can be attributed to the large, positive water-air temperature difference and little evaporative cooling at high humidity.

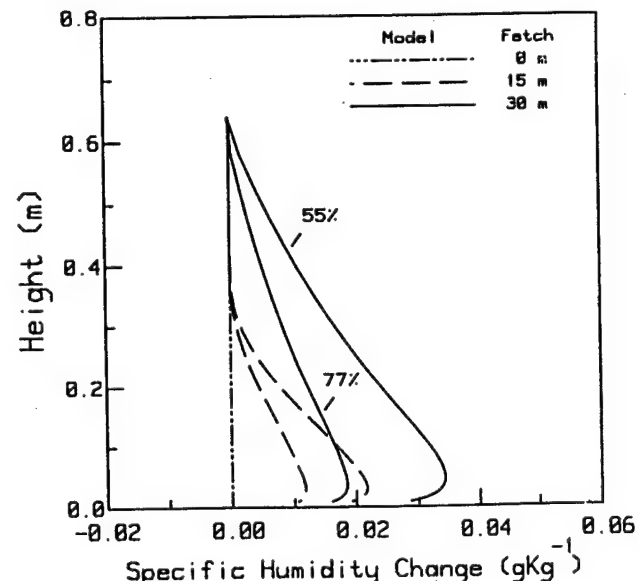


Figure 10. Profiles of the change in the model-derived specific humidity profiles due to the presence of droplets. The nominal wind speed was 7.5 m s^{-1} for all runs, while the relative humidity is as indicated on the profiles measured at 30 m (55% and 77%).

The lower-humidity runs shown in Figures 9 and 10 give the expected result of lower near-surface temperatures and higher specific humidities in the presence of droplets due to their evaporation. The magnitude of this change is similar to the results of *Rouault et al.* [1991], with a maximum of approximately 0.1°C in temperature and 0.05 g k g^{-1} in specific humidity. This is a barely measurable change (in fact, the precision of the sensors may not be able to resolve it) and is smaller than the measurements shown in Figure 16 in part 1. As stated in part 1, we believe that this is a consequence of droplets wetting the "dry-bulb" thermometer resulting in an underestimation of the dry-bulb temperature and overestimation of the specific humidity. For this reason we believe that the improvement in the model's performance is most likely due to the inclusion of the 2-D simulation of the mean temperature and humidity profiles, rather than the droplet feedback mechanism.

5.3. Influence of the Droplets on the Surface Energy Budget

On the basis of the results given in section 5.2, one might conclude that we should not expect droplets to have an appreciable effect on the surface energy budget. However, there are a number of reasons why this may not be the case for the marine boundary layer (MBL). For example, we have already shown that the intensity of uw in the LBL falls off rapidly with height. This decrease has a particularly adverse effect on large droplet dispersion as evidenced by Figures 7 and 8, where the majority of the potential moisture from the droplets is found below the highest height of 0.18 m, indicating that the largest droplets (which dominate the total water content) are rarely found above this level. This effect is also responsible for the reduction of the droplet concentration profile, as one moves 0.5 m downwind of their source, due to the rapid fallout of the largest droplets.

In fact, direct measurements of droplet profiles made from a wave follower by *De Leeuw* [1986, 1987] have shown that the gradient over the ocean is much smaller than that measured in the laboratory. While the mechanisms responsible for the enhanced mixing remain a hotly debated topic, it has been postulated that the reduced gradient may be the result of wave-induced motions and/or spume droplet production (e.g., see the discussion by *Wu* [1990] and *De Leeuw* [1990]). These spume drops are generated when spray is directly torn off the wave crests in high-wind conditions and are addressed in section 6.

Finally, in the CLUSE setup a droplet ejected at the tunnel entrance and kept aloft for the entire length of the test section (30 m) has approximately 4 s (at a nominal wind speed of 7.5 m s^{-1}) to interact with the turbulent fields of temperature and humidity. The work of *Andreas* [1990] has shown that droplets having an initial radius smaller than $20 \mu\text{m}$ are able to exchange 68% of their mass with the environment in 4 s. We can see the result of this exchange in Figure 10, where the contribution of the droplets to the moisture field increases significantly with fetch. However, this also means that much less than half of the droplet volume (found by integrating under

the curves in Figure 6) has a chance of contributing to the moisture field.

6. Marine Boundary Layer Simulation

The above discussion is particularly relevant to open ocean research because we have evidence that the source of droplets generated at IMST is representative of high-wind conditions over the open ocean. This is based on the comparison between the CLUSE source function and the estimates of the over-ocean function given by *Andreas* [1992] shown in Figure 11, which attempts to include the additional source of droplets arising from spume drop production. Figure 11 shows that the two functions are comparable for wind speeds between 15 and 18 m s^{-1} . The review by *Andreas et al.* [1995] placed this function on the high end of the most probable estimates of spray droplet production. Therefore this function is expected to maximize the influence of spray droplets on the near-surface energy budget, although even this assumption is far from certain due to our lack of knowledge concerning the generation of the largest (spume) drops.

In order to examine the influence of the droplets under high-wind conditions in the MBL, we conducted two separate simulations of a fully developed atmospheric surface layer using the *Andreas* [1992] source function. In both simulations we initialize Gwaihir with a constant flux layer using a 10-m wind speed U_{10} of 18 m s^{-1} , an air temperature of 20°C , a water temperature of 22°C , and a relative humidity of 80%. Periodic boundary conditions are used to allow the droplets to interact with the turbulent fields as long as they are airborne. The velocity is fixed at the upper boundary, while the temperature and humidity values are allowed to adjust so that the flux remains constant across the upper boundary. These conditions are specifically chosen for comparison with the analytical model results given by *Andreas et al.* [1995].

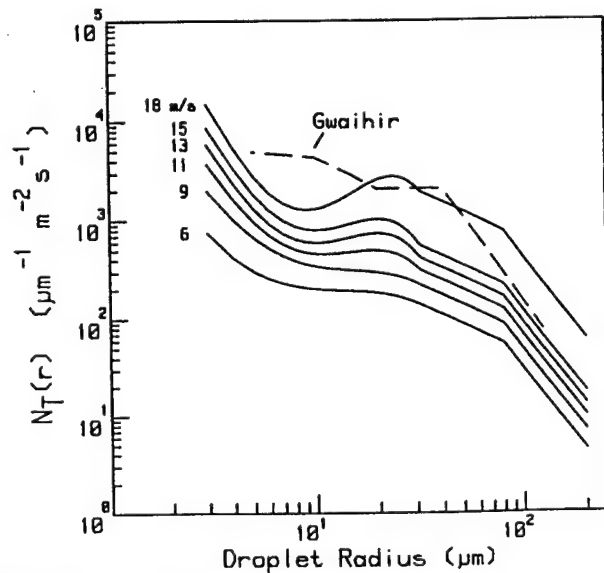


Figure 11. A comparison of the Gwaihir source function with the parameterization of the over ocean source function given by *Andreas* [1992].

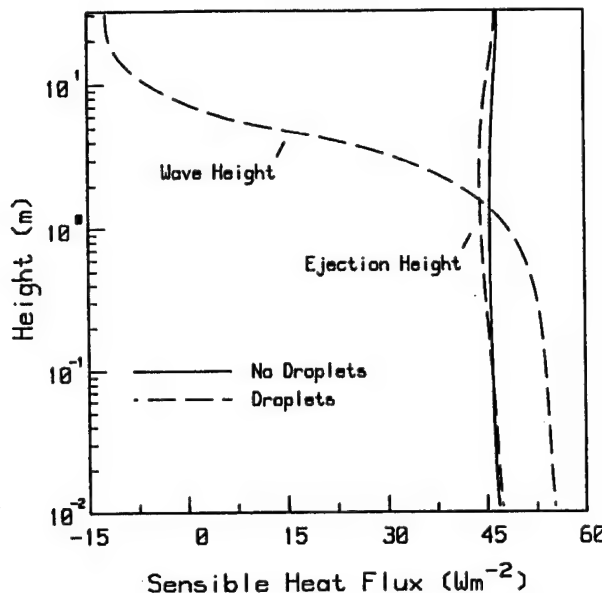


Figure 12. The model-derived sensible heat fluxes computed in the absence and presence of droplets released at two difference locations. The conditions during the run were a wind speed of 18 m s^{-1} and air temperature of 20°C at 10 m , a water temperature of 22°C , and a relative humidity of 80%.

The current version of Gwaihir does not attempt to directly model the influence of waves. However, we believe we can place some quantitative limits on the role they play in droplet dispersion and evaporative processes through the height at which we release the droplets. In the first simulation we release the droplets at their ejection height, while in the second simulation we release the droplets at the significant wave height determined by

$$A_{1/3} = 0.015 U_{10}^2 \quad (44)$$

The latter is intended to simulate a situation where the spume droplets are sheared off the wave crests and immediately find themselves at a considerable distance from the mean surface. Andreas [1992] has argued that $A_{1/3}(W^P)^{-1}$ is an appropriate timescale in his model, both because of the spume droplet effect and because it serves as a means to parameterize the increase of turbulence intensity with wind speed. However, because turbulent dispersion is already included in our model, we expect this simulation to give a best case scenario for droplet dispersion. This simulation should therefore approximate the upper bound on the possible droplet influence under these conditions. The release of the droplets from their ejection height is far less favorable for droplet dispersion and is expected to place a lower bound on the interactive processes for this particular source function.

The droplet's influence on the latent and sensible heat fluxes for the two runs are shown in Figures 12 and 13, where the fluxes are calculated from (9) and (10). The change to the mean humidity and temperature profiles are also shown in Figures 14 and 15 for comparison with the LBL results.

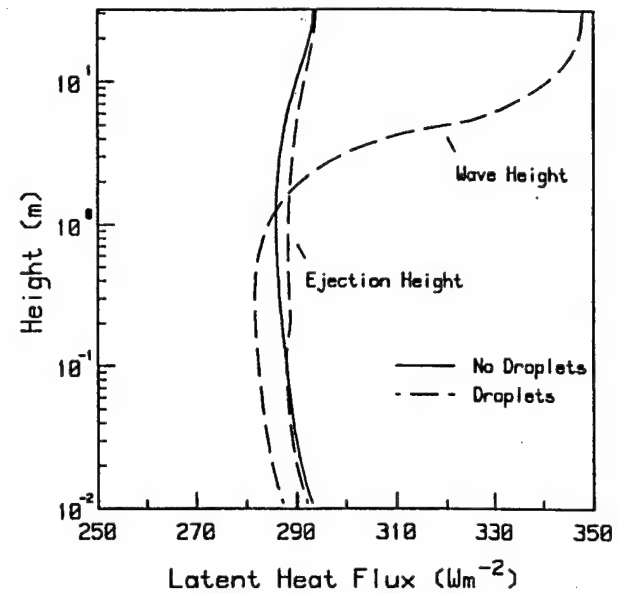


Figure 13. The model-derived latent heat fluxes computed in the absence and presence of droplets released at two difference locations. The conditions during the run are as in Figure 12.

Figures 12 through 15 show that the influence of droplet evaporation on the mean profiles and surface heat fluxes is strongly affected by the height at which the droplets are released.

The droplets released at their ejection height have a minimal impact on the latent and sensible heat fluxes and produce changes to the mean profiles that differ only slightly from the laboratory results. However, the droplets released at the wave

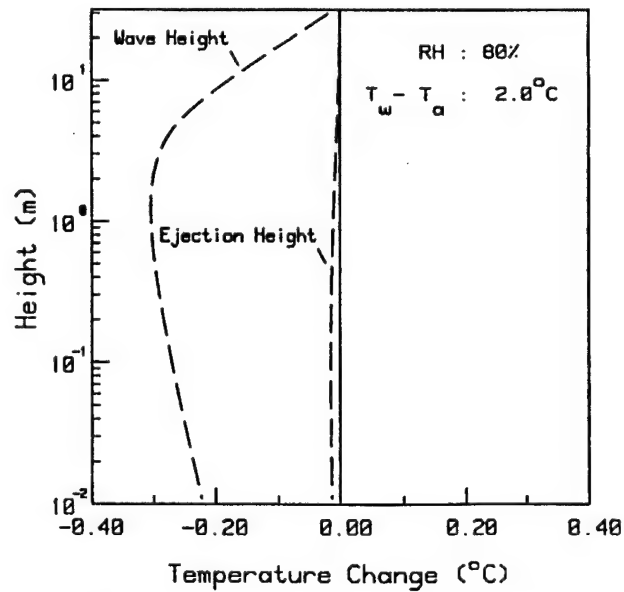


Figure 14. Profiles of the change in the model-derived temperature profiles due to the presence of droplets in our marine boundary layer (MBL) simulation. The conditions during the run were a relative humidity of 80% and a 10 m wind speed of 18 m s^{-1} .

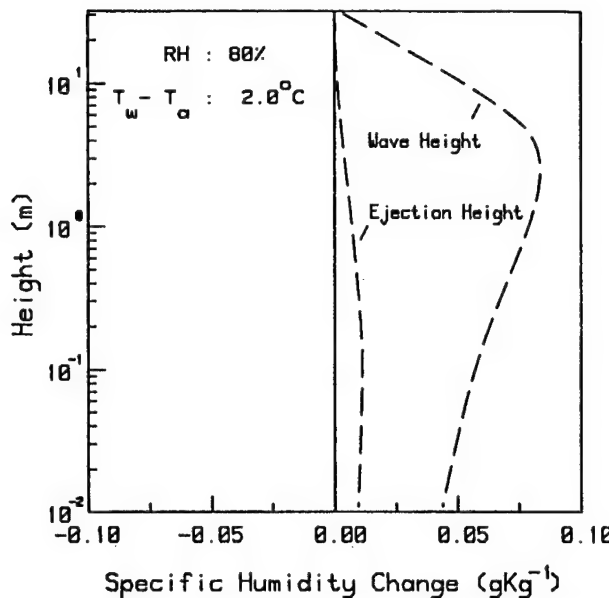


Figure 15. Profiles of the change in the model-derived specific humidity profiles due to the presence of droplets in our MBL simulation. The conditions during the run were a relative humidity of 80% and a 10-m wind speed of 18 m s^{-1} .

height (4.86 m in this simulation) significantly increase an already substantial latent heat flux by 20% at the top of model domain. The relatively weaker sensible heat flux is decreased by more than 100%. These finding agree very well with the results of *Andreas et al.* [1995], which found that the total droplet generated heat flux was roughly 30% of the interfacial (bulk) flux.

An interesting feature of these profiles is the apparent asymmetry of the droplet feedback effects described in part 1 and by *Andreas et al.* [1995]. These effects act to reduce the latent heat flux near the surface and increase it above. *Fairall et al.* [1995] hypothesized that this feedback could be included in the model of *Andreas* [1992] by assuming that only a fraction of the total droplet generated heat fluxes appears above the droplet evaporation layer. The asymmetry shown in Figures 12 and 13 suggests that this fraction is greater than the 50% used by *Fairall et al.* [1995].

7. Conclusions

In this paper we have shown that the Lagrangian model simulations given in part 1 have been even further improved by simply improving the simulation of the turbulent fields through which the droplets are dispersed. In the field, where it is difficult to measure even mean profiles near the surface, we can use the $k-\epsilon$ model to provide the required Lagrangian model parameters using measurements from the surface and at some reference height to initialize the Eulerian model. The droplet model can then be used to examine the influence of the droplet evaporation and sensible heat release on the surface energy budget using a variety of wind-dependent source functions once reliable field-based source function estimates are available.

Alternatively, Gwaihir could be used with the few near-surface profile measurements that are available to estimate the source function. This would be accomplished by adjusting the model source function until the modeled profiles match the measurements. The major problem with this approach is our lack of knowledge of how spume drops are produced over the ocean. This leads to a great deal of uncertainty in how to parameterize their production in numerical models. However, current research efforts focusing on spume drop production should improve these parameterizations in the near future.

Our results indicate that an increase in turbulence intensity due to high winds does not significantly increase the effect that evaporating jet droplets have on the scalar fields of temperature and humidity. The principal reason for this is that the turbulence is still not strong enough at the droplet's ejection height to overcome the fall velocity of the largest droplets. However, the potential for substantial modification of the surface heat fluxes exists if the presence of waves acts to eject the droplets higher, permitting the larger droplets to remain aloft for longer periods of time. Therefore we need to gain a better understanding of how the droplets are generated at high wind speeds (i.e., as spume and/or jet drops), as well as how the waves affect the dispersion of these droplets once airborne.

An initial attempt to study the waves effect has been reported by *Andreas et al.* [1995] using modifications to the model described in part 1. Although the relevance of these results as limited by the simplified flow field used to model the wave-induced velocity perturbations, these results clearly indicated that the presence of waves significantly increases the amount of vertical dispersion. Therefore the logical next step in the development of Gwaihir is to adapt it more fully to over-ocean conditions by introducing a wavy lower surface and using the $k-\epsilon$ model to simulate the flow field. We expect to produce a more accurate simulation of the flow over waves by using an approach similar to the modeling work of *Gent and Taylor* [1976].

Gwaihir will also have to determine a way to simulate the release of spume droplets if we wish to accurately model the effect of spray droplets under high-wind conditions. This might involve testing proposed source functions of spume droplets and releasing these droplets only at the wave crests. Of course, the inclusion of these droplets leads to a number of yet unresolved questions about their generation, such as the appearance of flow separation over breaking waves. However, we will leave those topics for future discussion.

Finally, the effects introduced by modeling droplets composed of seawater, rather than fresh water, would have to be included. This would primarily involve changes to the equations governing evaporation rate and determination of how to deal with the residual sea-salt droplet that remains behind after evaporation. Such droplets could have long residence times and are of importance in processes involving cloud physics and atmospheric optics.

Acknowledgments. Support for this research was provided by the National Science Foundation under grants INT-8907676 and OCE-9115227 and by the Centre National de la Recherche Scientifique. J.

Edson acknowledges support from the Office of Naval Research under grant N00014-95-1-0021 during the final preparation and publication of this article. This is Woods Hole Oceanographic Institution contribution 8794 and HEXOS contribution 47.

References

Andreas, E. L., Thermal and size evolution of sea spray droplets, *CRELL Rep. 89-11*, 37 pp., U.S. Army Cold Reg. Res. and Eng. Lab., Hanover, N.H., 1989.

Andreas, E. L., Time constants for the evolution of sea spray droplets, *Tellus, Ser. B.*, 42B, 481-497, 1990.

Andreas, E. L., Sea spray and the turbulent air-sea fluxes, *J. Geophys. Res.*, 97, 11,429-11,441, 1992.

Andreas, E. L., J. B. Edson, E. C. Monahan, M. P. Rouault, and S. D. Smith, The spray contribution to net evaporation from the sea: A review of recent progress, *Boundary Layer Meteorol.*, 72, 3-52, 1995.

Avva, R. K., S. J. Kline, and J. H. Ferziger, Computation of the turbulent flow over a backward-facing step using the zonal modeling approach, *Rep. TF-33*, Stanford Univ., Stanford, Calif., 1988.

Beard, K. V., and H. R. Pruppacher, A wind tunnel investigation of the rate of evaporation of small water drops falling at terminal velocity in air, *J. Atmos. Sci.*, 28, 1455-1464, 1971.

Blanchard, D. C., and A. H. Woodcock, Bubble formation and modification in the sea and its meteorological significance, *Tellus*, 9, 145-158, 1957.

Burk, S. D., The generation, turbulent transfer and deposition of the sea-salt aerosol, *J. Atmos. Sci.*, 41, 3040-3051, 1984.

Charnok, H., Wind stress on a water surface, *Quart. J. Roy. Meteorol. Soc.*, 81, 639, 1955.

Chorin, A. J., A numerical method for solving incompressible viscous flow problems, *J. Comput. Phys.*, 2, 12-26, 1967.

De Leeuw, G., Vertical profiles of giant particles close to the sea surface, *Tellus, Ser. B.*, 38B, 51-61, 1986.

De Leeuw, G., Near-surface particle size distribution profiles over the North Sea, *J. Geophys. Res.*, 92, 14,631-14,635, 1987.

De Leeuw, G., Comment on "Vertical distributions of spray droplets near the sea surface: Influence of jet drop ejection and surface tearing" by J. Wu, *J. Geophys. Res.*, 95, 9779-9782, 1990.

Duykerke, P. G., Application of the E- ϵ turbulence closure model to the neutral and stable atmospheric boundary layer, *J. Atmos. Sci.*, 45, 865-880, 1988.

Edson, J. B., and C. W. Fairall, Spray droplet modeling, 1, Lagrangian model simulation of the turbulent transport of evaporating droplets, *J. Geophys. Res.*, 99, 25,295-25,311, 1994.

Fairall, C. W., J. D. Kepert, and G. J. Holland, The effect of sea spray on the surface energy transports over the Ocean, *Atmos.-Ocean System*, in press, 1996.

Garratt, J. R., Review of drag coefficients over oceans and continents, *Mon. Weather Rev.*, 105, 915-917, 1977.

Gent, P. R., and P. A. Taylor, A numerical model of the airflow above water waves, *J. Fluid Mech.*, 77, 105-128, 1976.

Giovangeli, J.-P., and O. Le Calve, The structure of the atmospheric turbulent flow in the close vicinity of wind waves, in *Modelling the Fate and Influence of Marine Spray*, edited by P. G. Mestayer, E. C. Monahan, and P. A. Beetham, *Whitecap Rep.* 7, pp. 49-64, Mar. Sci. Inst., Univ. of Conn., Groton, 1990.

Hirt, C. W., and F. H. Harlow, A general corrective procedure for the numerical solution of initial value problems, *J. Comput. Phys.*, 2, 114-119, 1967.

Högström, U., Non-dimensional wind and temperature profiles in the atmospheric surface layer: A re-evaluation, *Boundary Layer Meteorol.*, 42, 55-78, 1988.

Katsaros, K. B., J. DeCosmo, R. J. Anderson, S. D. Smith, C. Kraan, W. A. Oost, L. Hasse, K. Bumke, P. G. Mestayer, and M. H. Smith, Measurements of humidity and temperature in the marine environment during the HEXOS main experiment, *J. Atmos. Ocean. Tech.*, 11(4), 964-981, 1994.

Lakehal, D., P. G. Mestayer, J. B. Edson, S. Anquetin, and J.-F. Sini, Eulero-Lagrangian simulation of atmospheric hydrometeor trajectories and impacts inside the urban canopy, *Atmos. Environ.*, in press, 1996.

Landahl, M. T., and E. Mollo-Christensen, *Turbulence and Random Processes in Fluid Mechanics*, 154 pp., Cambridge Univ. Press, New York, 1986.

Launder, B. E., and D. B. Spalding, The numerical computation of turbulent flows, *Comput. Methods Appl. Mech. Eng.*, 3, 269-289, 1974.

Lévi Alvarès, S., C. X. Zhang, and C. Sacré, Tests for a flow simulation around an isolated block: $k-\epsilon$ model improvements, paper presented at 9th Symposium on Turbulence and Diffusion, Am. Meteorol. Soc., Roskilde, Denmark, 1990.

Lévi Alvarès, S., Three-dimensional numerical simulation of turbulent flow around buildings using the $k-\epsilon$ model, Doctorate thesis, Lab. de Mec. des Fluides, Ecole Cent. de Nantes, France, 1992.

Lévi Alvarès, S., and J. F. Sini, Simulation of diffusion within an urban street canyon, *J. Wind Eng.*, 82, 114-119, 1992.

Ley, A. J., and D. J. Thomson, A random walk model of the dispersion in the diabatic surface layer, *Q. J. R. Meteorol. Soc.*, 109, 848-880, 1983.

Ling, S. C., and T. W. Kao, Parameterization of the moisture and heat transfer process over the ocean under whitecap sea states, *J. Phys. Oceanogr.*, 6, 306-315, 1976.

Ling, S. C., A. Saad, and T. W. Kao, Mechanics of multiphase fluxes over the ocean, in *Turbulent Fluxes through the Sea Surface, Wave Dynamics and Prediction*, edited by A. Favre and K. Hasselmann, pp. 185-197, Plenum, New York, 1978.

Ling, S. C., T. W. Kao, M. Asce, and A. Saad, Microdroplets and transport of moisture from the ocean, *J. Eng. Mech. Div. Am. Soc. Civ. Eng.*, 6, 1327-1339, 1980.

Meek, C. C., and B. G. Jones, Studies of the behavior of heavy particles in a turbulent flow, *J. Atmos. Sci.*, 30, 239-244, 1973.

Mestayer, P. G., De la structure fine des champs turbulents dynamique et thermique pleinement développés en couche limite, Thèse de Doctoratès-Sci. Phys., Univ. d'Aix-Marseille II, Marseille, France, 1980.

Mestayer, P. G., et al., CLUSE simulations of vapor flux transformations by droplet evaporation, in *Modelling the Fate and Influence of Marine Spray*, edited by P. G. Mestayer, E. C. Monahan, and P. A. Beetham, *Whitecap Rep.* 7, pp. 100-105, Mar. Sci. Inst., Univ. of Conn., Groton, 1990.

Mostafa, A. A., and H. C. Mongia, On the modeling of turbulent evaporating sprays: Eulerian versus Lagrangian approach, *Int. J. Heat Mass Transfer*, 12, 2585-2593, 1987.

Rouault, M. P., P. G. Mestayer, and R. Schiestel, A model of evaporating spray droplet dispersion, *J. Geophys. Res.*, 96, 7181-7200, 1991.

Selva, J.-P., Etude de l'influence de la stratification sur l'evaporation, Thèse de Doctorat de Eroisement Cycle, 173 pp., Inst. de Mec. Statist. de la Turbulence, Univ. d'Aix-Marseille II, Marseille, France, 1979.

Sini, J.-F., Modelisation d'écoulements turbulents libres bidimensionnels avec effets de flottabilité. Thèse de Doctorat de 3 me Cycle, 285 pp., Inst. de Mec. Statist. de la Turbulence, Univ. d'Aix-Marseille II, Marseille, France, 1986.

Sini, J.-F., and I. Dekéyser, Numerical prediction of turbulent plane jets and forced plumes by use of the k-e model of turbulence, *Int. J. Heat Mass Transfer*, 30, 1787-1801, 1987.

Snyder, W. H., and J. L. Lumley, Some measurements of particle velocity autocorrelation functions in a turbulent flow, *J. Fluid Mech.*, 48, 41-71, 1971.

Stramska, M., Vertical profiles of sea-salt aerosol in the atmospheric surface layer: A numerical model, *Acta Geophys. Pol.*, 35, 87-100, 1987.

Stull, R. B., *An Introduction to Boundary Layer Meteorology*, 666 pp., Kluwer Academic, Norwell, Mass., 1988.

Wells, M. R., and D. E. Stock, The effects of crossing trajectories on the dispersion of particles in a turbulent flow, *J. Fluid Mech.*, 136, 31-62, 1983.

Wu, J., Vertical distributions of spray droplets near the sea surface: Influence of jet drop ejection and surface tearing, *J. Geophys. Res.*, 95, 9775-9778, 1990.

S. Anquetin, Laboratoire des Ecoulements Géophysiques et Industriels, Université Joseph Fourier, Grenoble, France.
(email: anquetin@img.fr)

J. B. Edson, Department of Applied Ocean Physics and Engineering, Woods Hole Oceanographic Institution, Woods Hole, MA 02543. (e-mail: jedson@airsea2.whoi.edu)

P. G. Mestayer and J. F. Sini, Laboratoire de Mécanique des Fluides, Ecole Centrale de Nantes, Nantes, France.
(e-mail: mestayer@ecn01.ec-nantes.fr)

(Received April 10, 1995; revised July 12, 1995;
accepted July 21, 1995.)

P20.4 MODELING THE ROLE OF SEA SPRAY ON AIR-SEA HEAT AND MOISTURE EXCHANGE

James B. Edson
Woods Hole Oceanographic Institution, Woods Hole, Massachusetts

Edgar L. Andreas
U.S. Army Cold Regions Research and Engineering Laboratory, Hanover, New Hampshire

1. INTRODUCTION

Ocean scientists have been speculating for about 50 years that sea spray droplets can enhance the air-sea fluxes of heat and moisture. The literature in this field, however, has yielded no consensus one way or the other. One of the major problems involves the uncertainty surrounding the source function for these droplets. The number of droplets produced at the sea surface is known to be a function of both droplet size and environmental conditions. However, the various source functions proposed in the literature spans several order of magnitude. Once the spray droplets are airborne, the principal concern of modelers is to determine a realistic means to simulate the interaction between the evaporating droplets and the temperature and moisture fields.

Droplets at the small end of the size spectrum remain suspended indefinitely and thus can exchange all the heat and water vapor they have available. But because of the number produced and their size, these small droplets do not contribute much to the air-sea heat and moisture fluxes. Large droplets, on the other hand, carry a lot of heat and moisture but fall back into the sea so quickly that they do not contribute much to the surface fluxes either. The mid-range droplets -- those with radii at formation between 10 and 200 μm (mostly spume droplets) -- thus contribute most to the air-sea fluxes because they are small enough to remain suspended for a few seconds and also carry a moderate amount of heat and moisture.

Individually, we have developed two distinct models for the role of sea spray in air-sea heat and moisture exchange. Details about the models can be found in Andreas (1990, 1992), Edson and Fairall (1994), and Edson et al. (1996). Therefore, we only provide a brief description of our models in the following section and then focus on two test comparisons. These two comparisons are chosen to simulate conditions where we might expect significant spume droplet production: a moderate-wind-speed case (10 m/s) over the tropical Pacific, and a high-wind-speed case (18 m/s) at mid-latitudes.

2. THE MODELS

Andreas's (1992) model has three components. First, it predicts that rate at which sea spray droplets with initial radii between 2 and 500 μm are produced at the sea surface as a function of wind speed. This spray generation function is derived from Miller's (1987) generation function but also has the first realistic prediction for spume production. Spume droplets are those torn directly off the wave crests by the wind, are typically 20 μm in radius and larger, and contribute most to the spray sensible and latent heat fluxes (Andreas 1992).

Corresponding author address: J.B. Edson, WHOI MS#10, 98 Water St., Woods Hole, MA 02543, jedson@whoi.edu

The second component of Andreas's (1992) spray model is a complete microphysical model that computes, for droplets of arbitrary size, time scales that quantify how rapidly individual droplets exchange sensible and latent heat with their environment (Andreas 1990). By comparing these time scales with an estimate of a droplet's residence time above the sea surface, the model can estimate how much of a droplet's available heat and water it can exchange before falling back into the sea. The third component of Andreas's spray model is thus an estimate of this residence time, parameterized as the quotient of the significant wave amplitude and the droplet's settling speed in still air.

Edson's model consists of two interactive components (Edson et al., 1996). The first component is an Eulerian k - ϵ model of turbulent flows that closes the system of equations using two prognostic equations for the turbulent kinetic energy, k , and its rate of dissipation, ϵ . The second component is a Lagrangian model of evaporating sea spray (Edson and Fairall, 1994). The Lagrangian model keeps track of the amount of sensible heat and moisture absorbed or released in each cell of the Eulerian domain during each step of a droplet's trajectory. This determines the source/sink terms for the prognostic equations of temperature and moisture in the Eulerian model. The two models are then run iteratively until a steady state is reached.

3. RESULTS

In this initial comparison, Edson's model attempts to include the presence of waves by simply releasing the droplets at the same significant wave amplitude used by Andreas (1992). The model also imposes constant flux conditions at the top of the model domain, periodic lateral boundary conditions, and constant surface roughness at the lower boundary. The same source function is used in both models.

Edson's model is able to predict the sensible and latent heat flux profiles in the absence (H_s and H_L) and presence (F_s and F_L) of spray droplets. The profiles of H_s and H_L are shown by the solid lines in Figs. 1 and 2, while profiles of F_s and F_L are shown by the broken lines for the two simulations. Andreas's model computes H_s and H_L and the nominal spray sensible (Q_s) and latent (Q_L) heat fluxes. The two models can be compared using

$$F_s = H_s + \beta Q_s + \alpha Q_L - \gamma Q_L \quad (1)$$

$$F_L = H_L - \alpha Q_L \quad (2)$$

where α , β , and γ are small, non-negative numbers. The γ term accounts for possible feedback effects. We should also point out that Andreas (1992) computes Q_L as negative

because droplets must consume latent heat to evaporate. Andreas (1992) implicitly assumed $\alpha = \beta = 1, \gamma = 0$. Fairall et al. (1994) tried $\alpha = \beta = 0.5, \gamma = 0$ in a model examining spray droplet effects in tropical storms. We examine these particular constants in the comparisons summarized by Table 1.

4. CONCLUSIONS

Our two models compare reasonably well in both cases. In particular, both predict that, for the high wind speed case, the spray latent heat flux, especially, will be at least 10% of the normal turbulent or interfacial latent heat flux. In other words, sea spray can significantly enhance the air-sea heat and moisture fluxes in high winds. Our modeling also suggests how to partition the total air-sea sensible and latent heat fluxes into contributions from turbulent and spray fluxes. We are now working on the inclusion of a wavy lower boundary in the Eulerian code. We would then release the droplets at their (jet droplet) ejection height along the wave to obtain a more realistic simulation of the influence of the waves. If successful, we believe that we will be able to develop a simple parameterization of the spray heat fluxes for use in large-scale models.

This work is supported by the Office of Naval Research.

5. REFERENCES

Andreas, E. L., 1990: Time constants for the evolution of sea spray droplets. *Tellus*, **42B**, 481- 497.
 Andreas, E. L., 1992: Sea spray and the turbulent air-sea heat fluxes. *J. Geophys. Res.*, **97**, 11429-11441.
 Edson, J.B. and C.W. Fairall, 1994. Spray droplet modeling, I: Lagrangian model simulation of the turbulent transport of evaporating droplets. *J. Geophys. Res.*, **99**, 25295-25311.
 Edson, J.B., S. Anquetin, P.G. Mestayer, and J.F. Sini, 1996. Spray droplet modeling II: An interactive Eulerian-Lagrangian model of evaporating spray droplets, *J. Geophys. Res.*, **101**, 1279-1294.
 Fairall, C.W., J.D. Kepert and G.J. Holland, 1994: The effect of sea spray on surface energy transports over the ocean. *Global Atmos. Ocean Sys.*, **2**, 121-142.
 Miller, M. A., 1987: An Investigation of Aerosol Generation in the Marine Planetary Boundary Layer. M.S. thesis,

Department of Meteorology, Pennsylvania State University, University Park, 142 pp.

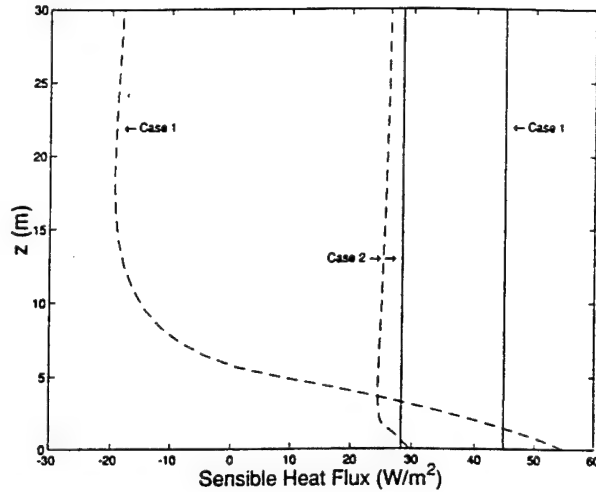


Fig.1 Profiles of the sensible heat flux computed in the absence (solid line) and presence (broken line) of droplets.

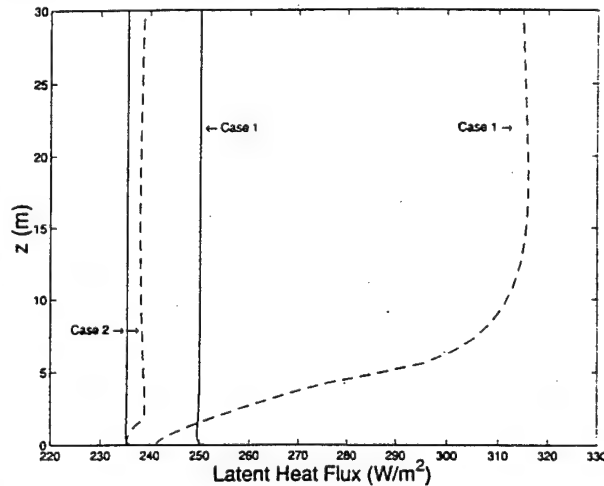


Fig.2 Profiles of the latent heat flux computed in the absence (solid line) and presence (broken line) of droplets.

Table 1. Comparison of our model results under environmental conditions commonly experienced during autumn in Mid-Latitudes and during westerly wind bursts in the Tropical Pacific.

Flux Variable	Case 1: "Mid-Latitude"			Case 2: "Tropical Pacific"		
	Andreas	Edson ($\alpha, \beta=1, \gamma=0$)	Edson ($\alpha, \beta=0.5, \gamma=0$)	Andreas	Edson ($\alpha, \beta=1, \gamma=0$)	Edson ($\alpha, \beta=0.5, \gamma=0$)
$U_{10} = 18 \text{ m/s}; T_{air} = 20^\circ\text{C}; T_{sea} = 22^\circ\text{C}; \text{RH} = 80\%$						$U_{10} = 10 \text{ m/s}; T_{air} = 27^\circ\text{C}; T_{sea} = 29^\circ\text{C}; \text{RH} = 80\%$
$H_s (\text{W/m}^2)$	41.7	44.9	44.9	26.5	28.3	28.3
$H_L (\text{W/m}^2)$	243.4	250.1	250.1	224.3	235.5	235.5
$Q_s (\text{W/m}^2)$	6.9	1.6	3.2	0.9	0	0.1
$Q_L (\text{W/m}^2)$	-62.4	-65.9	-131.8	-4.4	-2.6	-5.2

James Edson and Suzanne Wetzel
Woods Hole Oceanographic Institution, Woods Hole, Massachusetts

Carl Friehe, Scott Miller and Tihomir Hristov
University of California, Irvine, California

1. INTRODUCTION

Investigations of atmospheric turbulence over the world's oceans have shown that the interaction of wind with surface waves results in flow characteristics that differ substantially from even a horizontally homogeneous surface layer over land. As a result, marine meteorologists and physical oceanographers often divide the boundary layer close to the surface into the surface layer where Monin-Obukhov (MO) similarity holds, and a wave boundary layer (WBL) where additional scaling parameters are required for similarity. Even though the search for these scaling parameters and hypotheses for their use has been going on for many years (e.g., Miles, 1957; Hare et. al, 1997), we are still a long way from a consensus in the scientific community.

In this paper we present some of our on-going investigations of turbulence and wave-induced flow in the marine surface layer. These investigations rely on a set of data collected from the R/P FLIP during the Marine Boundary Layers (MBL) experiment sponsored by the Office of Naval Research. Specifically, this paper examines the energy flux and its relationship to its rate of dissipation within the marine boundary layer. The flux of kinetic energy, $F(z)$, into a layer of air over a horizontally homogeneous surface is given by

$$F(z) = \overline{u'w'}U(z) + \overline{v'w'}V(z) + \overline{w'e'} + \frac{1}{\rho} \overline{w'p'} \quad (1)$$

where the first two terms on the right-hand-side represents the flux of mean flow kinetic energy, and the second two represent the rate of diffusion of kinetic energy. Over land, we often assume that the energy flux through the ground is negligible, such that the flux entering the layer at height h can be related to the total rate of dissipation within the layer by

$$\int_0^h \epsilon dz = -F(h) + \frac{g}{T_v} \int_0^h \overline{w'T_v'} dz \quad (2)$$

where the second term on the right-hand-side accounts for the generation of kinetic energy due to any buoyancy flux. For neutral conditions, this expression states that the flux of kinetic energy into a layer is balanced by the total rate of dissipation within that layer.

Over the ocean, we expect the surface energy flux, which drives waves and currents, to be non-negligible. Expression

Corresponding author address: J.B. Edson, WHOI MS#10, 98 Water St., Woods Hole, MA 02543, jedson@whoi.edu

(2) must be modified to take into account the energy into the ocean, $F(0)$, such that

$$\int_0^h \epsilon dz = -[F(h) - F(0)] + \frac{g}{T_v} \int_0^h \overline{w'T_v'} dz \quad (3)$$

Therefore, less volume averaged dissipation is required to balance the same energy flux into the layer as long as there is a net flux into the ocean. In fact, the difference between the integrated dissipation rate and the total energy flux at the top of this layer can be used to roughly estimate the energy flux into the ocean.

2. SIMILARITY THEORY

In a stationary, horizontally homogenous, constant stress layer, the vertical derivative of the energy flux takes the form of the familiar TKE budget equation

$$\epsilon = -\frac{\overline{u'w'}\partial U}{\partial z} - \frac{\overline{v'w'}\partial V}{\partial z} - \frac{\partial \overline{w'e'}}{\partial z} - \frac{1}{\rho} \frac{\partial \overline{w'p'}}{\partial z} + \frac{g}{T_v} \overline{w'T_v'} \quad (4)$$

MO scaling provides us with a dimensionless form of the TKE budget given by

$$\Phi_\epsilon \left(\frac{z}{L} \right) = \frac{\epsilon \kappa z}{u_*^3} = \Phi_m \left(\frac{z}{L} \right) - \Phi_e \left(\frac{z}{L} \right) - \Phi_p \left(\frac{z}{L} \right) - \frac{z}{L} \quad (5)$$

where L is the MO length, κ is the von Karman constant, and u_* is the friction velocity. This expression is often used to estimate the momentum over the ocean from estimates of the dissipation rates and a parameterization of Φ_ϵ from

$$\rho u_*^2 = \rho [\epsilon \kappa z / \Phi_\epsilon(z/L)]^{2/3} \quad (6)$$

This type of parameterization should be valid as long as the measurements are made above the WBL and the constant flux assumption holds. However, an additional forcing mechanism is introduced due to the presence of surface waves as we approach the surface. In this region (i.e., the WBL), MO similarity is expected to break down. For example, in the WBL the velocity can be decomposed into mean, turbulent, and wave-induced components

$$u(t) = U + u'(t) + \bar{u}(t) \quad (7)$$

where the wave-induced component is defined using an extension of Reynolds averaging known as phase averaging (e.g., Finnegan et al., 1984).

This type of averaging can be used to rewrite the TKE energy budget to include the wave-induced components. For example, the shear production, P , would include terms representing the energy production due to the interaction between the wave-induced flux and the mean shear

$$P = -\overline{u'w'}[1 + \overline{u\bar{w}}/\overline{u'w'}]\frac{\partial U}{\partial z} - \overline{v'w'}[1 + \overline{v\bar{w}}/\overline{v'w'}]\frac{\partial V}{\partial z} \quad (8)$$

The bracketed terms are not expected to obey M-O scaling, which leads to a breakdown of similarity relationships like (5) within the WBL.

3. RESULTS AND CONCLUSIONS

Even if we are able to separate the wave-induced fluctuations from the turbulence, a scale analysis of even a simplified form of kinetic energy equation is a difficult task. However, we can begin to make some inferences about the behavior of the combined fluctuations and their related fluxes (i.e., the total flux) using the data collected during the MBL experiment. The data collected from the FLIP mast allows us to compute all the terms of the total kinetic energy flux at 2-3 levels, and the dissipation rate of TKE at 4 levels.

We begin our discussion with a comparison of our ϵ measurements with their MO similarity prediction

$$\epsilon_p = \frac{u_*^3}{kz} \phi_e(z/L) = \frac{u_*^3}{kz} [\phi_m(z/L) - z/L] \quad (9)$$

where we assume a balance between production and dissipation for ϕ_e , i.e., we have not attempted to parameterize the transport terms. We expect (9) to be greater than our measured values as long as there is a net flux into the ocean. Evidence for this is shown in Fig. 1, which shows that the measured dissipation profiles are less than the M-O prediction. These profiles were averaged over a period of increasing winds and growing seas. The "dissipation deficit" becomes smaller as, presumably, we move out of the WBL.

We attempt to reconcile the difference between the predicted and measured dissipation rates by considering the underlying sea-state in Fig. 2. In this figure, we have normalized our dissipation estimates by (9) and then bin-averaged according to the indicated ranges of the wave-age parameter, c/u_* ; and kz , where k is the wavenumber of the dominant waves defined from the peak of the wave spectra.

Our dissipation estimates are adequately predicted by MO similarity theory for mature seas above $kz \approx 1.5$. However, our results also indicate that there is an appreciable difference between our dissipation measurements and their MO predictions for all sea-states when $kz < 1$. The dissipation deficit is greatest over the youngest sea as one would intuitively expect. Therefore, our results indicate that the dissipation rate does not obey M-O similarity within the WBL, and that the dissipation deficit appears to be a function of sea-state.

We are now investigating whether the dissipation deficit

is balanced by the transport of energy to the surface and/or by a modification of the energy production due to the presence of waves (see abstracts by Hare et al., Hristov et al., and Miller et al. in this volume). Our findings have important implications for use of the inertial dissipation and bulk aerodynamic methods over the ocean, particularly from buoys. The influence of the surface waves on the near surface turbulence is significant and a means to account for their presence should be included in subgrid-scale parameterizations in LES and lower boundary conditions in numerical models.

This work was supported by the Office of Naval Research.

4. REFERENCES

Finnegan, J.J., F. Einaudi, and D. Fu, 1984: The interaction between an internal gravity wave and turbulence in the stably-stratified nocturnal boundary layer. *J. Atmos. Sci.*, **41**, 2409-2436.
 Hare, J.E., T. Hara, J.B. Edson, and J.M. Wilczak, 1997: A similarity analysis of the structure of air flow over surface waves. *J. Phys. Oceanogr.*, in press.
 Miles, J.W., 1957: On the generation of surface waves by shear flows. *J. Fluid Mech.*, **3**, 185-204.

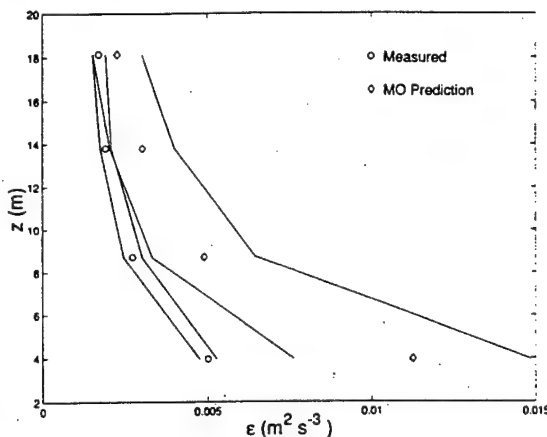


Fig. 1. Measured and predicted dissipation profiles averaged over a 4 hour period.

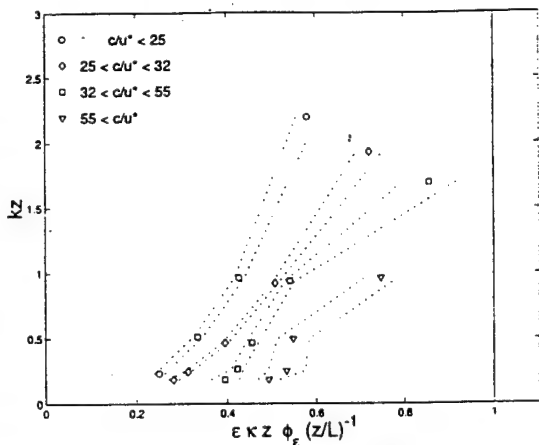


Fig. 2. Bin-averaged normalized dissipation profiles.

P11.3 STRUCTURE OF THE ATMOSPHERIC SURFACE LAYER OVER THE OCEAN WAVES — PHASE AVERAGING VIA THE HILBERT TRANSFORM

T. Hristov*, C. Friehe*, S. Miller*, J. Edson**, S. Wetzel**

*Department of Mechanical and Aerospace Engineering, University of California at Irvine, Irvine, CA 92697-3975

**Woods Hole Oceanographic Institution, Woods Hole, MA 02543

April 14, 1997

1 INTRODUCTION

Recent advancements in the technology of the experiment made it possible to collect high quality field data sets, which contain better information about the coupling between the wind and the waves and can be used to approach in a new way longstanding problems related to wind-waves interaction. All this stimulates the development of new methods for data processing and analysis. In this paper we present and apply such a new method. The data analyzed here are from the Marine Boundary Layer Experiment, which took place in April-May 1995 50 kilometers off the coast of California. The instrumentation used in this analysis includes a vertical array of sonic and cup anemometers for horizontal and vertical velocity measurements, and a wave wire situated directly beneath this array to compute the necessary wave statistics.

The air flow over ocean waves is conveniently decomposed into mean, turbulent and wave coherent components $u = \bar{u} + u_{turb} + \tilde{u}$. The separation is made by the origin of the components, but also more importantly, by the fact that the coupling between these components is weak enough. The wave coherent component is the one responsible for the exchange of momentum and energy between the waves and air flow. That is why its identification from field experiment data is of primary interest.

To approach the identification problem we can assume that the turbulent component in the air flow and the wave are not correlated. Let us consider monochromatic waves with a period T_0 and the air flow velocity at a certain height above the point where the wave height is measured. Under the assumptions above, averaging the air flow velocity for a number of periods N ,

$$\tilde{u}_{T_0}(t) = \hat{\mathcal{S}}u(t) \equiv \left(\frac{1}{N} \sum_{n=1}^N u(t + nT_0) \right) - \bar{u}, \quad (1)$$

should filter out the turbulence and what will be left is the phase average of the wave coherent component [1, 2]. If the waves are monochromatic such a technique should perform well. However, the waves in the open ocean are spread over an interval of spectral scales and the attempt to use (1) with field data, leads to strong attenuation of the phase average as a result of destructive interference [3]. This motivated the development of a different approach, which would be much less sensitive to the lack of coherence in nonmonochromatic wave fields.

2 PHASE AVERAGING VIA THE HILBERT TRANSFORM

Just to introduce the idea, let us recall that a signal which consists of two Fourier components $A_1 e^{i\omega_1 t}$ and $A_2 e^{i\omega_2 t}$ has instantaneous amplitude $A(t)$ and phase $\varphi(t)$ formed by the rule $A(t)e^{i\varphi(t)} = A_1 e^{i\omega_1 t} + A_2 e^{i\omega_2 t}$. For a signal of arbitrary spectrum $s(t)$, the idea can be generalized by employing the concept of the analytic signal based on the Hilbert transform [4]. The analytic signal $\Psi(t)$ is a complex-valued function of time defined as

$$\Psi(t) = s(t) + is_H(t) = A(t)e^{i\varphi(t)}, \quad (2)$$

where the function $s_H(t)$ is the Hilbert transform of $s(t)$

$$s_H(t) = \hat{\mathcal{H}}s(t) \equiv \frac{1}{\pi} \mathcal{P} \int_{-\infty}^{\infty} \frac{s(\tau)}{t - \tau} d\tau, \quad (3)$$

and \mathcal{P} indicates that the integral is taken in the sense of the Cauchy principal value. From (3), the Hilbert transform $s_H(t)$ of $s(t)$ may be seen as the convolution of the functions $s(t)$ and $1/\pi t$. For the frequencies of interest in physics $\omega > 0$, the Fourier transforms of $s(t)$ and $s_H(t)$ satisfy $S_H(\omega) = -iS(\omega)$; i.e., ideally $s_H(t)$ may be obtained from $s(t)$ by a filter whose amplitude response is unity, and whose phase response is $\pi/2$ lag at all frequencies [4].

Let $\eta(t)$ be the wave height signal over a time interval T and let $u(t)$ be the wind velocity, measured above the point, where the wave height is measured. Let $\Psi(t) = \eta(t) + i\eta_H(t)$ and $\Phi(t) = \text{Arg}\Psi(t)$ be the wave's instantaneous phase, as defined above. Then, to select and average the wind velocities at the moments τ when the wave phase $\Phi(\tau) = \Phi(t)$, we can use the transformation

$$\hat{\mathcal{P}}u(t) \equiv \frac{\int_0^T u(\tau) \Phi'(\tau) \delta(\Phi(\tau) - \Phi(t)) d\tau}{\int_0^T \Phi'(\tau) \delta(\Phi(\tau) - \Phi(t)) d\tau} - \bar{u}. \quad (4)$$

For monochromatic signals $\eta(t)$, (4) is equivalent to (1). For nonmonochromatic experimental signals, $\hat{\mathcal{S}}$ and $\hat{\mathcal{P}}$ show very different results (Fig. 1).

3 DISCUSSION

We can use $\hat{\mathcal{P}}u(t)$ as a strictly periodic approximation of the wave coherent component in the wind $\tilde{u}(t)$ to calculate the wave coherent momentum and energy fluxes. Let $\tilde{u}(t) \equiv (\tilde{u}(t), \tilde{v}(t), \tilde{w}(t))$ be approximated by $\hat{\mathcal{P}}u(t) = \{\tilde{u}_0 \cos(\omega_0 t + \phi_u), \tilde{v}_0 \cos(\omega_0 t + \phi_v), \tilde{w}_0 \cos(\omega_0 t + \phi_w)\}$, and

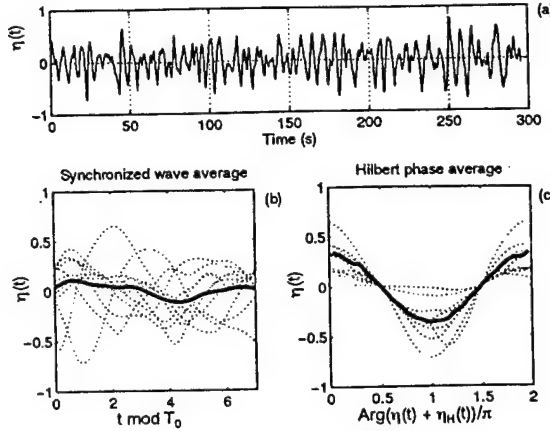


Figure 1: A wave height signal vs. time (a), its synchronized average $\hat{S}\eta(t)$ (b) and Hilbert-transform phase average $\hat{P}\eta(t)$ (c). In (b) and (c) the dotted lines show the original signal. The period of the most energetic mode T_0 is the length of the subintervals in (b). Due to destructive interference, the average $\hat{S}\eta(t)$ of 10 periods is attenuated and distorted (b). In contrast, $\hat{P}\eta(t)$ on (c) shows no attenuation or distortions.

the wave coherent air pressure fluctuations on the interface $\tilde{p}(t)$ by $\hat{P}p(t) = \tilde{p}_0 \cos(\omega_0 t + \phi_p)$, where all the phases are referenced to the phase of $\hat{P}\eta(t) = \eta_0 \cos \omega_0 t$ and ω_0 is an appropriate frequency. Then the wave coherent stress $\langle \tilde{u}(t) \tilde{w}(t) \rangle$ and the energy flux $\langle \tilde{p}(t) \partial \eta(t) / \partial t \rangle$ are

$$\langle \hat{P}u(t) \hat{P}w(t) \rangle = 0.5 \tilde{u}_0 \tilde{w}_0 \cos(\phi_u - \phi_w) \quad (5)$$

$$\langle \hat{P}p(t) \partial \hat{P}\eta(t) / \partial t \rangle = 0.5 \omega_0 \eta_0 \tilde{p}_0 \sin(\phi_p). \quad (6)$$

The results (5) and (6) make obvious, that the phase differences control the direction of the momentum and energy fluxes and suggest that representing the structure of the surface layer in terms of amplitudes and phases of the phase averaged wave coherent fields $\hat{P}u(t)$, $\hat{P}p(t)$, etc., would be descriptive and adequate. The phase shift between the wave coherent components in the air flow and the wave itself indicates a separation of the air flow [5, 6, 7, 8], which now can be detected and measured by using the transformation \hat{P} from open ocean experiment data. Figure 2 shows two results obtained with the phase averaging technique we just described.

4 CONCLUSION

In conclusion, we presented a robust approach allowing to separate the turbulent and wave coherent components in the air flow over surface waves. The technique makes it possible to identify flow separation and to estimate the exchange of momentum and energy between the air flow and the waves from field experiments. The method also allows to detect inverted momentum and energy fluxes for decaying seas — a phenomenon predicted by models, but not observed in open ocean experiments.

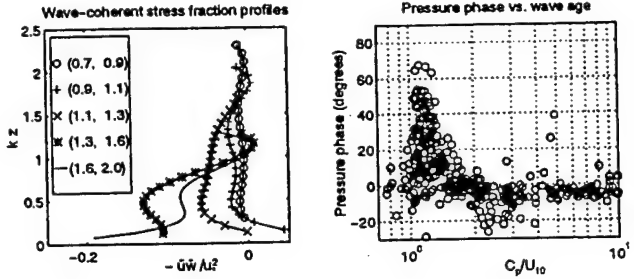


Figure 2: The left plot represents the profiles of the wave-coherent stress as a fraction of the total stress $-\langle \tilde{u}\tilde{w} \rangle / u_*^2$. Each profile corresponds to a different wave age C_p/U_{10} , (C_p is the waves' phase speed and U_{10} is the mean wind speed at 10 meters) as shown on the legend. The sign of the stress is chosen to be positive for momentum flux downwards. The profiles confirm that for developing seas most of the wave coherent stress occurs close to the surface and is positive. For large wave ages the wave induced stress represents a considerable fraction of the total stress and is negative (upwards). The plot on the right shows the phase offset of the pressure fluctuations vs. wave age C_p/U_{10} . For low wave ages the pressure is lagging the wave (the cluster of positive pressure phases), so the waves grow. For larger wave ages (waves out-running the wind), the pressure is leading the waves (higher pressure before the wave), which makes the waves to decay. The sensor measuring the pressure fluctuations was positioned 12 meters above the surface.

Acknowledgements

The work was supported by the Office of Naval Research under grant N00014-93-1-0923. We would like to thank the crew of the FLIP and the Marine Physical Laboratory for their assistance, and Lloyd Green of the Scripps Institution of Oceanography for the wave wire array and Jim Wilczak of NOAA for the pressure sensors.

References

- [1] C. H. D. Buys-Ballot. *Les Changements Périodiques de Température Dépendants de la Nature du Soleil et de la Lune* ... Kremink & Fils, Utrecht, 1847.
- [2] J. J. Finnigan, F. Einuadi, and D. Fua. The interaction between internal gravity wave and turbulence in the stably-stratified nocturnal boundary layer. *J. Atmos. Sci.*, 41(16):2409–2436, 1984.
- [3] S. Wetzel, J. B. Edson, C. Friehe, T. Hristov, and S. Miller. An investigation of wave-induced momentum flux through phase averaging of open ocean wind and wave fields. to be published.
- [4] W. Gardner. *Statistical Spectral Analysis, a Nonprobabilistic Theory*. Prentice Hall, Englewood Cliffs, NJ, 1988.
- [5] H. Jeffreys. On formation of waves by wind. *Proc. Roy. Soc.*, A107:189–206, 1924.
- [6] G. J. Komen, L. Cavaleri, M. Donelan, K. Hasselmann, S. Hasselmann, and P. A. M. Janssen. *Dynamics and Modelling of Ocean Waves*. Cambridge University Press, Cambridge, 1994.
- [7] S. Belcher and J. C. R. Hunt. Turbulent shear flow over slowly moving waves. *J. Fluid Mech.*, 251:109–148, 1993.
- [8] C. Mastenbroek, V. K. Makin, M. H. Garat, and G. P. Giovanangeli. Experimental evidence of the rapid distortion of turbulence in the air flow over water waves. *J. Fluid Mech.*, 318:273–302, 1996.

6. Continuing work on the simulation of the flow of air over ocean waves.

The Langrangian and coupled models have been validated in the large air-sea interaction simulation tunnel at IMST, Luminy, France. As such, the model has been shown to perform well in simulations of a developing boundary layer over a roughened surface. Since that time, the PIs efforts have focused on inclusion of a wavy lower boundary layer in the Eulerian code. This section summarizes these efforts.

Spray droplet modeling 3. Simulating droplet dispersion over ocean waves

James B. Edson

Woods Hole Oceanographic Institution

1. Introduction

Spray droplets are produced over the ocean by bubbles bursting at the surface. These bubbles are usually produced by the air entrained by breaking waves. These bubble-generated spray droplets generally fall under two categories: film droplets that arise from the breakup of the leading side of the bubble (i.e., the bubble film) as it penetrates the surface, and jet droplets that result from the breakup of the column of water (i.e., the jet) ejected from the collapsing bubble cavity. This production mechanism also accounts for the generation of spray droplets produced by rain striking the surface. Sea spray known as spume droplets are also produced through direct shearing of the wave crests under high wind conditions. Therefore, except in instances of rain under light winds, these spray droplets are ejected into the wave boundary layer (WBL) where wave-induced motions are a significant component of the velocity field. As such,

the dispersion of these droplets is expected to be influenced by the presence of waves.

2. Model Summary

In developing equations designed to study flows where the mean departure from hydrostatic equilibrium can be nonzero (e.g., around a building), *Sini* [1986] and *Sini and Dekeyser* [1987] decomposed this departure from hydrostatic equilibrium into mean and fluctuating parts. This approach is also well-suited for simulating the airflow over waves as the pressure field is expected to be out of local hydrostatic equilibrium. Application of the Boussinesq approximation results in Reynolds averaged equations for the mean variables given by

$$\frac{\partial \overline{U}_j}{\partial x_j} = 0 \quad (1)$$

$$\frac{\partial \overline{U}_i}{\partial t} + \overline{U}_j \frac{\partial \overline{U}_i}{\partial x_j} = -\frac{1}{\overline{\rho}_a} \frac{\partial \overline{P}}{\partial x_i} - g_i \frac{\overline{\Theta}_v - \overline{\Theta}_v^r}{\overline{\Theta}_v^r} - \frac{\partial \overline{u}_i \overline{u}_j}{\partial x_j} + v \frac{\partial^2 \overline{U}_i}{\partial x_j^2} \quad (2)$$

$$\frac{\partial \overline{\Theta}}{\partial t} + \overline{U}_j \frac{\partial \overline{\Theta}}{\partial x_j} = \frac{\partial \overline{u}_j \overline{\Theta}}{\partial x_j} + \frac{S_H}{\overline{\rho}_a c_p} \quad (3)$$

and

$$\frac{\partial \overline{Q}}{\partial t} + \overline{U}_j \frac{\partial \overline{Q}}{\partial x_j} = \frac{\partial \overline{u}_j q}{\partial x_j} + S_q \quad (4)$$

where Einstein's summation notation is used; the overbar represents an ensemble average; lower

case letters denote the turbulent fluctuations; ν is the kinematic viscosity; Θ_v is the ambient virtual potential temperature; Θ_v^r is the virtual potential temperature of the reference state of the fluid; Q is the total specific humidity; $g_i = (0,0,-g)$ where g is the gravitational acceleration; ρ_a is the density of air; c_p is the specific heat at constant pressure; and S_H and S_q represent source terms for sensible heat and moisture, respectively. These source/sink terms simulate the exchange of sensible and latent heat between the evaporating droplets and the scalar fields as they are dispersed in the surface layer.

2.1. Closure

The Reynolds-stress tensor is modeled using a slightly modified form of the Boussinesq eddy diffusivity concept to allow for anisotropy (see *Taylor*, 1977 for the isotropic forms)

$$-\overline{uw} = \nu_T \left(\frac{\partial \bar{U}}{\partial z} + \frac{\partial \bar{W}}{\partial x} \right) \quad (5)$$

$$e - \sigma_u^2 = \nu_T \left(\frac{\partial \bar{U}}{\partial x} - \frac{\partial \bar{W}}{\partial z} \right) \quad (6)$$

$$\frac{e}{3} - \sigma_w^2 = \nu_T \left(\frac{\partial \bar{W}}{\partial z} + \frac{\partial \bar{U}}{\partial x} \right) \quad (7)$$

$$\frac{2e}{3} - \sigma_v^2 = 0 \quad (8)$$

where σ_u , σ_v , and σ_w are the standard deviations of the longitudinal, lateral, and vertical velocity fluctuations, respectively; ν_T is the eddy diffusivity; and e is the turbulent kinetic energy (TKE) defined as

$$e = \frac{1}{2} \bar{u_j u_j} \quad (9)$$

In first-order closure models the eddy diffusivity in a neutral surface layer is parameterized as

$$v_T = \kappa z u_* \quad (10)$$

where u_* is the friction velocity and κ is the von Karman constant, which we assign the value 0.4. In our $e-\epsilon$ closure model, the eddy diffusivity is parameterized as

$$v_T = C_\mu \frac{e^2}{\epsilon} \quad (11)$$

where ϵ is the dissipation rate of TKE and C_μ is a model coefficient. The model coefficient can be determined using the near-surface relationship for the dissipation rate under neutral conditions

$$\epsilon = \frac{u_*^3}{\kappa z} \quad (12)$$

which results in

$$C_\mu = \frac{u_*^4}{e^2} \quad (13)$$

Our modifications to the Boussinesq concept approximates the empirical results given in *Panofsky and Dutton (1984)* such that

$$\sigma_u^2 \approx e \equiv 6 u_*^2 \quad \sigma_v^2 \approx \frac{2}{3} e \equiv 4 u_*^2 \quad \sigma_w^2 \approx \frac{1}{3} e \equiv 2 u_*^2 \quad (14)$$

Using these values the numerical constant becomes $C_u = 1/36$. The scalar fluxes are then modeled using

$$-\overline{u_j \theta} = Pr_T v_T \frac{\partial \overline{\theta}}{\partial x_j} \quad (15)$$

$$-\overline{u_j q} = Sc_T v_T \frac{\partial \overline{q}}{\partial x_j} \quad (16)$$

where the Prandtl and Schmidt numbers for turbulent diffusion are assigned the same value, $Pr_T = Sc_T = 0.95$ [Högström, 1988].

Closure is then accomplished through prognostic equations for both the TKE and its rate of dissipation

$$\frac{\partial e}{\partial t} + \overline{U_j} \frac{\partial e}{\partial x_j} = -\overline{u_i u_j} \frac{\partial \overline{U_i}}{\partial x_j} - \frac{g_j}{\Theta_v} \overline{u_j \theta_v} + \frac{\partial}{\partial x_j} \left[v_T \frac{\partial e}{\partial x_j} \right] - \epsilon \quad (17)$$

$$\frac{\partial \epsilon}{\partial t} + \overline{U_j} \frac{\partial \epsilon}{\partial x_j} = -C_{\epsilon 1} \frac{\epsilon}{k} \left[\overline{u_i u_j} \frac{\partial \overline{U_i}}{\partial x_j} + \frac{g_j}{\Theta_v} \overline{u_j \theta_v} \right] + \frac{\partial}{\partial x_j} \left[v_T \frac{\partial \epsilon}{\partial x_j} \right] - C_{\epsilon 2} \frac{\epsilon^2}{e} \quad (18)$$

where σ_ϵ , $C_{\epsilon 1}$, σ_ϵ , and $C_{\epsilon 2}$ are additional model coefficients. These coefficients are derived using the expressions in *Edson et al.* (1996) that provide the values summarized in Table 1. The production terms in the above equations are also modified by the inclusion of terms that normally cancel by invoking continuity. For example, the production term in the TKE equation can be written out as

$$-\overline{u_i u_j} \frac{\partial \overline{U_i}}{\partial x_j} = v_T \left(\frac{\partial \overline{U}}{\partial z} + \frac{\partial \overline{W}}{\partial x} \right)^2 + v_T \left(\frac{\partial \overline{U}}{\partial x} - \frac{\partial \overline{W}}{\partial z} \right)^2 - e \left(\frac{\partial \overline{U}}{\partial x} + \frac{1}{3} \frac{\partial \overline{W}}{\partial z} \right) \quad (19)$$

where the last term on the right hand side is normally neglected when the isotropic form of the

Reynold stress tensor is used.

Table 1. Numerical constants used in present model.							
C_μ	$C_{\epsilon 1}$	$C_{\epsilon 2}$	σ_e	σ_ϵ	κ	Pr_T	Sc_T
0.03	1.44	1.92	1.0	2.0	0.4	0.95	0.95

2.2 Model Modifications for the Undulating Surface

The $e-\epsilon$ model described by *Edson et al.* (1996) requires a number of modifications to simulate the flow over ocean waves. An obvious difficulty in using the set of equations given above is how to define the velocity, temperature, humidity fields when z is beneath the wavy surface. One commonly used method to get around this problem involves setting up a new, wave following coordinate system (χ, Z) where

$$\begin{aligned}\chi &= x \\ Z &= z - \eta e^{-k\zeta}\end{aligned}\tag{20}$$

where η is the instantaneous wave height and k is the principle wavenumber of the undulating surface. This coordinate system has the desirable characteristics that $z = \eta$ when $Z = 0$, and $z \approx Z$ for $Z > k$. As in *Taylor* (1977), we assume that the flow is well represented by logarithmic velocity profiles and transform Z to a logarithmic vertical coordinate ζ as

$$\zeta = \ln(Z)\tag{21}$$

The set of governing equations can be rewritten for the (χ, ζ) coordinate system using the

relationships

$$\frac{\partial \phi}{\partial x} = \frac{\partial \phi}{\partial \chi} + \frac{1}{Z} \frac{\partial \phi}{\partial \zeta} \frac{\partial Z}{\partial x} \quad (22)$$

$$\frac{\partial \phi}{\partial z} = \frac{1}{Z} \frac{\partial \phi}{\partial \zeta} \frac{\partial Z}{\partial z} \quad (23)$$

$$\frac{\partial^2 \phi}{\partial x^2} = \frac{\partial^2 \phi}{\partial \chi^2} + \frac{2}{Z} \frac{\partial^2 \phi}{\partial \chi \partial \zeta} \frac{\partial Z}{\partial x} + \frac{1}{Z^2} \frac{\partial^2 \phi}{\partial \zeta^2} \left(\frac{\partial Z}{\partial x} \right)^2 + \frac{1}{Z} \frac{\partial \phi}{\partial \zeta} \frac{\partial^2 Z}{\partial x^2} \quad (24)$$

$$\frac{\partial^2 \phi}{\partial z^2} = \frac{1}{Z^2} \frac{\partial^2 \phi}{\partial \zeta^2} \left(\frac{\partial Z}{\partial z} \right)^2 + \frac{1}{Z} \frac{\partial \phi}{\partial \zeta} \frac{\partial^2 Z}{\partial z^2} \quad (25)$$

where ϕ represents the appropriate velocity, temperature or humidity variable in our set of equations.

2.3 Initialization and Boundary Conditions

The height of the domain is chosen such that $z_{\max} = 3/k$. Periodic boundary conditions are used at the lateral boundaries. A stokes wave is chosen for the lower boundary

$$\eta(\chi) = -\frac{H_w}{2} \cos(k\chi - \omega t) + \frac{H_w^2}{8} k \cos(2(k\chi - \omega t))$$

where ω is the angular frequency and H_w is the wave height. In order to reach steady-state conditions, we require the total momentum flux to be constant with height within the model domain such that

$$\frac{\partial \tau(z)}{\partial z} = 0 = \rho \frac{\partial}{\partial z} \left(-\overline{u'w'} - \overline{\tilde{u}\tilde{w}} + v \frac{\partial \overline{U}}{\partial z} \right) \quad (27)$$

where v is the kinematic viscosity and the primes and tildas denote turbulent and wave induced fluctuations, respectively [i.e., $U(t) = \overline{U} + u(t) = \overline{U} + u'(t) + \tilde{u}(t)$]. The last term on the right hand side of (26) represents the viscous shear stress and is accounted for in the model by adding v to our parameterization of v_T . The initial wind profiles throughout the model domain are defined in a frame of reference moving with the phase speed of the dominate wave, c_p , such that

$$\overline{U}(\zeta, \chi) - c_p = U_s + U_w(\chi) e^{-k\zeta} + \frac{u_*}{\kappa} \ln \left[\frac{\zeta + \zeta_o}{\zeta_o} \right] - c_p \quad (28)$$

$$\overline{W}(\zeta, \chi) = \left[\frac{\partial \eta}{\partial t} + (U_s + U_w(\chi)) \frac{\partial \eta}{\partial x} \right] e^{-k\zeta} \quad (29)$$

where $U_w(\chi) = k \eta(\chi) c_p$ is the wave orbital velocity, and U_s is the surface drift current. At the upper boundary where the wind speed is fixed at

$$\overline{U}_{\max} - c_p = U_s + \frac{u_*}{\kappa} \ln \left[\frac{z_{\max} + \zeta_o}{\zeta_o} \right] - c_p \quad (30)$$

$$\overline{W}_{\max} = 0 \quad (31)$$

The initial simulations rely on the dispersion relationship for deep water waves to provide the relationships

$$\omega = \frac{g}{c_p} \quad , \quad k = \frac{\omega}{c_p} \quad (32)$$

The wave height, phase speed, surface roughness, and drift current are parameterized using

$$H_w = 0.015 * U_{10} , \quad \frac{c_p}{U_{10}} = 1.2 , \quad \zeta_o = \beta \frac{u_*^2}{g} + \frac{v}{9u_*} , \quad U_s = \frac{u_*}{\kappa} \quad (33)$$

where $U_{10} = \overline{U}(\zeta = 10)$ and β is the Charnock constant, which is assigned the value of 0.011.

Therefore, the model is initialized by choosing a value for U_{\max} , iteratively solving (31) for u_* , and computing the phase speed and wave height from $U_{10} = U_s + u_* / \kappa \ln(10/\zeta_o)$. This value of the friction velocity defines the constant value of the total momentum flux throughout the domain as

$$\tau = -\rho \overline{uw} = \rho u_*^2 \quad (34)$$

3. Work in Progress

The remaining component of the model that needs to be properly parameterized is the energy and momentum flux boundary conditions, and the effects of the wave-induced energy flux divergence. The momentum flux going into the waves (i.e., the form drag) is given by

$$-\rho \overline{\tilde{u}\tilde{w}}_o \approx \overline{p_o \frac{\partial \eta}{\partial x}} \quad (35)$$

where the pressure-slope correlation represents the momentum flux supported by the entire spectrum of waves. The present model can only resolve the form drag due to the dominate wave. Therefore, the question arises how to take into account the unresolved component of the form drag. Our model simple assumes that the total momentum flux minus the resolvable form drag must be balanced by the shear stress

$$u_*^2 - \frac{1}{\rho} \left(\overline{p_o \frac{\partial \eta}{\partial z}} \right)_r = (v_T + v) \left(\frac{\partial \overline{U}}{\partial z} + \frac{\partial \overline{W}}{\partial x} \right) \quad (36)$$

The mean wind at the first grid point is then assigned the appropriate value to provide this balance.

Another difficulty involves the non-zero energy flux at the surface. This flux is mainly carried by the wave induced pressure-vertical velocity correlation at the surface

$$E_o \approx \overline{\tilde{w}\tilde{p}}_0 \approx \overline{p_o \frac{\partial \eta}{\partial t}} \quad (37)$$

which again is partially resolved by our model. Therefore, our initial simulations assume that the total energy flux minus the resolvable flux must be balanced by the diffusive flux

$$E_o - \left(\overline{p_o \frac{\partial \eta}{\partial t}} \right)_r = \frac{v_T}{\sigma_e} \frac{\partial e}{\partial z} \quad (38)$$

which provides the value of the kinetic energy at the lowest grid point. The total energy flux is parameterized using

$$E_o = \int_{-\infty}^{\infty} \gamma S(k) dk$$

where γ is the wave input term (e.g., Plant, 1982) and $S(k)$ is the wave spectrum. The divergence of this flux plus the wave induced energy flux appears in the kinetic energy budget as

$$\frac{\partial}{\partial z} \left[\frac{\overline{\tilde{w}\tilde{p}}}{\rho} + \overline{\tilde{w}\tilde{e}} \right] \quad (40)$$

At present, only the divergence of the turbulent components are accounted for in (17). Therefore, proper simulation of the flow over waves must find a method to properly account for these effects. Several methods have been presented in the literature (e.g., *Makin and Mastenbroek, 1996; Mastenbroek et al., 1996*). We are now starting to compare our model simulations with

measurements from the 1995 Marine Boundary Layers program to see if any these methods or some new approach can provide adequate agreement with our observations.

4.0 References

Edson, J.B., S. Anquetin, P.G. Mestayer, and J.F. Sini, Spray droplet modeling 2. An interactive Eulerian-Lagrangian model of evaporating spray droplets, *J. Geophys. Res.*, 101, 1279-1294, 1996.

Högström, U., Non-dimensional wind and temperature profiles in the atmospheric surface layer: A re-evaluation, *Boundary Layer Meteorol.*, 42, 55-78, 1988.

Makin, V. K., and C. Mastenbroek, Impact of waves on air-sea exchange of sensible heat and momentum, *Boundary Layer Meteorol.*, 79, 279-300, 1996.

Mastenbroek, C., V. K. Makin, M. H. Garat, and J. P. Giovanangeli, Experimental evidence of the rapid distortion of turbulence in the air flow over water waves, *J. Fluid Mech.*, 318, 273-302, 1996.

Panofsky, H. A. and J. A. Dutton, *Atmospheric Turbulence*, New York, John Wiley and Sons, 1984.

Plant, W. J., A relation between wind stress and wave slope, *J. Geophys. Res.*, 87, 1961-1967, 1982.

Sini, J.-F., and I. Dekeyser, Numerical prediction of turbulent plane jets and forced plumes by use of the k-e model of turbulence, *Int. J. Heat Mass Transfer*, 30, 1787-1801, 1987.

Sini, J.-F., Modelisation d'écoulements turbulents libres bidimensionnels avec effets de flottabilité. Thèse de Doctorat de 3^{me} Cycle, 285 pp., Inst. de Mec. Statist. de la Turbulence, Univ. d'Aix-Marseille II, Marseille, France, 1986.

Taylor, P. A., Some numerical solutions of surface boundary-layer flow over gentle topography, *Boundary Layer Meteorol.*, 11, 439-465, 1977.

REPORT DOCUMENTATION PAGE			Form Approved OMB No. 0704-0188
<p>Public reporting burden for this collection of information is estimated to average 1 hour per response, including the time for reviewing instructions, searching existing data sources, gathering and maintaining the data needed, and completing and reviewing the collection of information. Send comments regarding this burden estimate or any other aspect of this collection of information, including suggestions for reducing this burden, to Washington Headquarters Services, Directorate for Information Operations and Reports, 1215 Jefferson Davis Highway, Suite 1204, Arlington, VA 22202-4302, and to the Office of Management and Budget, Paperwork Reduction Project (0704-0188), Washington, DC 20503.</p>			
1. AGENCY USE ONLY (Leave blank)	2. REPORT DATE	3. REPORT TYPE AND DATES COVERED	
		Final: 10/15/94 - 10/14/96	
4. TITLE AND SUBTITLE		The Impact of Evaporating Sea-Spray Droplets on the Surface Energy Budget Under High Wind Speeds Over Waves.	
6. AUTHOR(S)		James B. Edson	
7. PERFORMING ORGANIZATION NAME(S) AND ADDRESS(ES)		8. PERFORMING ORGANIZATION REPORT NUMBER	
Woods Hole Oceanographic Institution 96 Water Street Woods Hole, MA 02543			
9. SPONSORING/MONITORING AGENCY NAME(S) AND ADDRESS(ES)		10. SPONSORING/MONITORING AGENCY REPORT NUMBER	
Office of Naval Research Code 252A: SDH Ballston Tower One 800 N. Quincy Street Arlington, VA 22217-5660			
11. SUPPLEMENTARY NOTES			
12a. DISTRIBUTION/AVAILABILITY STATEMENT		12b. DISTRIBUTION CODE	
Approved for public release; distribution is unlimited			
13. ABSTRACT (Maximum 200 words)			
<p>The project involved an investigation of the effects of evaporating sea-spray under high wind conditions. These investigations were accomplished using a interactive Eulerian-Lagrangian model developed by the PI. The interactive model was validated using data collected during the 1988 CLUSE program. This work has demonstrated that the combined model accurately simulates the turbulent transport of evaporating droplets. In additions, this paper advanced the state-of-the-art in droplet research by demonstrating that the potential for substantial modification of the surface energy budget exists if the presence of waves acts to eject the droplets higher and/or disperse the droplets more efficiently. The model predicted that the contribution of the sea spray on the latent heat flux is at least 10% of the total under high wind speed conditions. The second part of this investigation has involved modifications to the Eulerian portion of the code to include a wavy lower boundary. The validation of this model is being accomplished through comparisons with an open ocean data set collected aboard the R/P FLIP during the 1995 Marine Boundary Layers Experiment. These observations are now being used to improve the boundary conditions and closure schemes to simulate the flow over waves as realistically as possible.</p>			
14. SUBJECT TERMS			15. NUMBER OF PAGES 35
Sea-Spray droplets, surface energy, marine boundary layer, lower boundary			16. PRICE CODE
17. SECURITY CLASSIFICATION OF REPORT	18. SECURITY CLASSIFICATION OF THIS PAGE unclassified	19. SECURITY CLASSIFICATION OF ABSTRACT unclassified	20. LIMITATION OF ABSTRACT UL

NSN 7540-01-280-5500

Standard Form 298 (Rev. 2-89)
Prescribed by ANSI Std. Z39-18
298-102